SOLFEO

ESA Contract No 4000127610/19/I-NS

Final report

Date of issue: 21 October 2020

Authors:

Ronald van der A, Jenny Stavrakou, Jean-François Müller, Maite Bauwens, Jieying Ding

Table of Contents

List of Acronyms

ATBD	Algorithm Theoretical Baseline Document
CAMS	Copernicus Atmospheric Monitoring Service
CTM	Chemical Transport Model
DECSO	Daily Emission estimation Constrained by Satellite Observations
EDGAR	Emission Database for Global Atmospheric Research
ECMWF	European Centre for Medium-range Weather Forecasts
FTIR	Fourier Transform InfraRed
GEIA	Global Emission InitiAtive
GFAS	Ground Fire Acquisition System
GFED	Global Fire Emission Database
GFS	Global Forecast System
HTAP	Hemispheric Transport of Air Pollution
IASI	Infrared Atmospheric Sounding Interferometer
IGAC	International Global Atmospheric Chemistry
MAGRITTE	Model of Atmospheric composition at Global and Regional scales using Inversion Techniques for Trace gas Emissions
MAX-DOAS	Multi AXis Differential Optical Absorption Spectroscopy
MEGAN	Model of Emissions of Gases and Aerosols from Nature
MERRA	Modern-Era Retrospective analysis for Research and Applications
MetOp	Meteorological Operational Satellite Program of Europe
OMI	Ozone Monitoring Instrument
PAPILA	Prediction of Air Pollution In Latin America
SAOZ	Systeme d'Analyse par Observations Zenithale
SOLFEO	Spaceborne Observations over Latin America For Emissions Optimization applications
TROPOMI	Tropospheric Monitoring Instrument
QA4ECV	Quality Assurance for Essential Climate Variables

1 Introduction

South America is one of the less studied continents in terms of air quality and emissions of hydrocarbons. Emission inventories that are in use for South America are either global (HTAP inventory) or consist of the various national inventories. In addition, a few local emission inventories exist that are focusing on specific megacities, but a detailed South-American inventory is not existing yet. Initiatives like EMISA (Emission Inventories in South America), an IGAC activity, are currently trying to improve this situation by stimulating the development of emission inventories using a bottom-up approach. This is challenging since emissions from the agricultural regions and the Amazon rain forest are poorly known. Knowledge of the emission distribution and magnitude in the Amazon region is essential, t since it is the largest source of natural hydrocarbons released into the atmosphere. These emissions are also changing rapidly since the forest undergoes continuous pressure due to increasing needs for pasture and agricultural land and the growth of nearby megacities.

Satellites provide timely observations over the entire region of South America with constant quality. In SOLFEO we are using these satellite observations to derive emission estimates of key pollutants in the region. Relevant environmental topics in South America are deforestation, forest fires, soil quality (for agricultural yields) and air quality. For studying these topics it is important to closely monitor both the natural emissions released by the rainforest (hydrocarbons, especially isoprene) and the rapidly changing anthropogenic emissions from agricultural and fossil fuel burning, resulting in ammonia (NH_3) and nitrogen-oxides (NO_x) emissions (Table 1).

Table 1 Emissions per topic

Environmental topic	Relevant emission
Air quality (traffic and industry)	Nitrogenoxide
Deforestation	Isoprene
Eutrophication	Ammonia, nitrogenoxide
Fires (forest or agricultural)	Hydrocarbons, ammonia, nitrogenoxide
Soil quality (due to fertilizers and livestock)	Ammonia, nitrogenoxide
Vegetation stress	Isoprene

The derived space-borne emissions are of interest for scientific users (e.g. PAPILA, GEIA), national governments in South America, agricultural organizations (e.g. AAPRESID), environmental organizations for air quality or forest protection, or international initiatives like EMISA.

By using satellite observations combined with a state-of-the-art model representation of the relevant processes, we have developed advanced inversion algorithms for the estimation of emissions. Based on our vast experience in inversion algorithms we developed the MAGRITTE adjoint code for deriving hydrocarbon emission fluxes, and in particular isoprene, from observations of the satellite instruments OMI (on AURA) and TROPOMI (on Sentinel 5p). NO_x emissions are derived using the existing DECSO algorithm but for the first time applied to TROPOMI observations. A new branch of DECSO has been developed to derive ammonia (NH_3) emissions from observations of the satellite instruments IASI (on MetOp) and CrIS (on Suomi NPP). The inversion algorithms are described in detail in chapter 2, 3 and 4.

Validation is a difficult aspect of emissions since direct flux measurements on the ground are rather sparse. That is why comparisons are often made with existing bottom-up inventories or modelled concentrations resulting from the derived emissions are compared to local ground observations. Techniques to check the internal consistency of the space-based emissions have also been developed.

Table 2 Validation data

Emissions	Validated against:
Ammonia	Global inventory HTAP and a Argentinian national inventory (section 2)
Hydrocarbons	Ground-based data (FTIR) and other inventories (GFED, GFAS). (section 5)
Isoprene	Aircraft observations, flux measurements, and various bottom-up inventories (section 5)
Nitrogen dioxide	Global inventory HTAP, TNO emissions (CAMS-related) and an Argentinian national inventory (section 4)

2 Agricultural emissions from IASI NH_3 observations (WP2)

The NH_3 emissions parallelly increase with human population and fertilizer usage over the past century. The excessive anthropogenic emissions of N compound to the environment has a major effect on the global biogeochemical N cycle which may result in adverse climate change, health effect and the reduction in biodiversity. Thus, the emission information of NH_3 is very important to study its impact on environment, human health and climate change and related environmental control strategy for both scientists and policy makers.

The empirical method to calculate the NH_3 emissions is called the bottom-up approach, which is based on statistics on emission activities and emission factors. In South America, NH_3 emissions derived from this approach have high uncertainties due to the lack of information on emission activities. With the help from a CTM and data assimilation techniques, the NH_3 emissions can be estimated from the satellite observations.

The existing DECSO algorithm from KNMI can be applied to NH_3 observations from space to estimate NH_3 emissions, which will provide a more accurate spatial and temporal distribution of total NH_3 surface emissions. The satellite observations from IASI on the MetOp satellites provide global maps of NH_3 concentration. In this project, we use the NH_3 observations from IASI to estimate NH_3 emissions.

2.1 IASI instrument

IASI is an infrared Fourier transform spectrometer. The first IASI has been on board MetOp-A since October 2006. A second one was launched on MetOp-B in September 2012. Both satellites fly in a polar Sun-synchronous orbit with overpass times at 9:30 and 21:30 local time. IASI has a square field of view, which is composed of four circular footprints of 12km each at nadir, distorted to ellipse-shaped pixels off-nadir. In this study, we use the ANNI-NH3-v2.1R-I retrieval product (Van Damme et al., 2017) from Université Libre de Bruxelles (ULB). This is the reanalysis version of ANNI-NH3-v2.1R using input generated from the ECMWF ERA-Interim dataset and a surface temperature retrieved by a secondary neural network. The analysis of ANNI-NH3-v2.1 time series revealed several rather sharp discontinuities which seemed to coincide with IASI L2 version changes. The ANNI-NH3-v2.1R-I is self-consistent in time and is expected to be highly suitable to study long-term trends.

Dammers et al. (2019) and Van Damme et al. (2018) estimated NH_3 emissions from point sources using the same NH3 retrieval product. The previous versions of the NH_3 product were validated by Dammers et al. (2016) and were found to have a low bias of about 40% and with better performance for the regions with high concentrations. Van Damme et al. (2017) stated that the ANNI NH3 v2.1 reanalysis retrieval product used for NH_3 emission estimates is self-consistent in time and is expected to be highly suitable to study long-term trends.

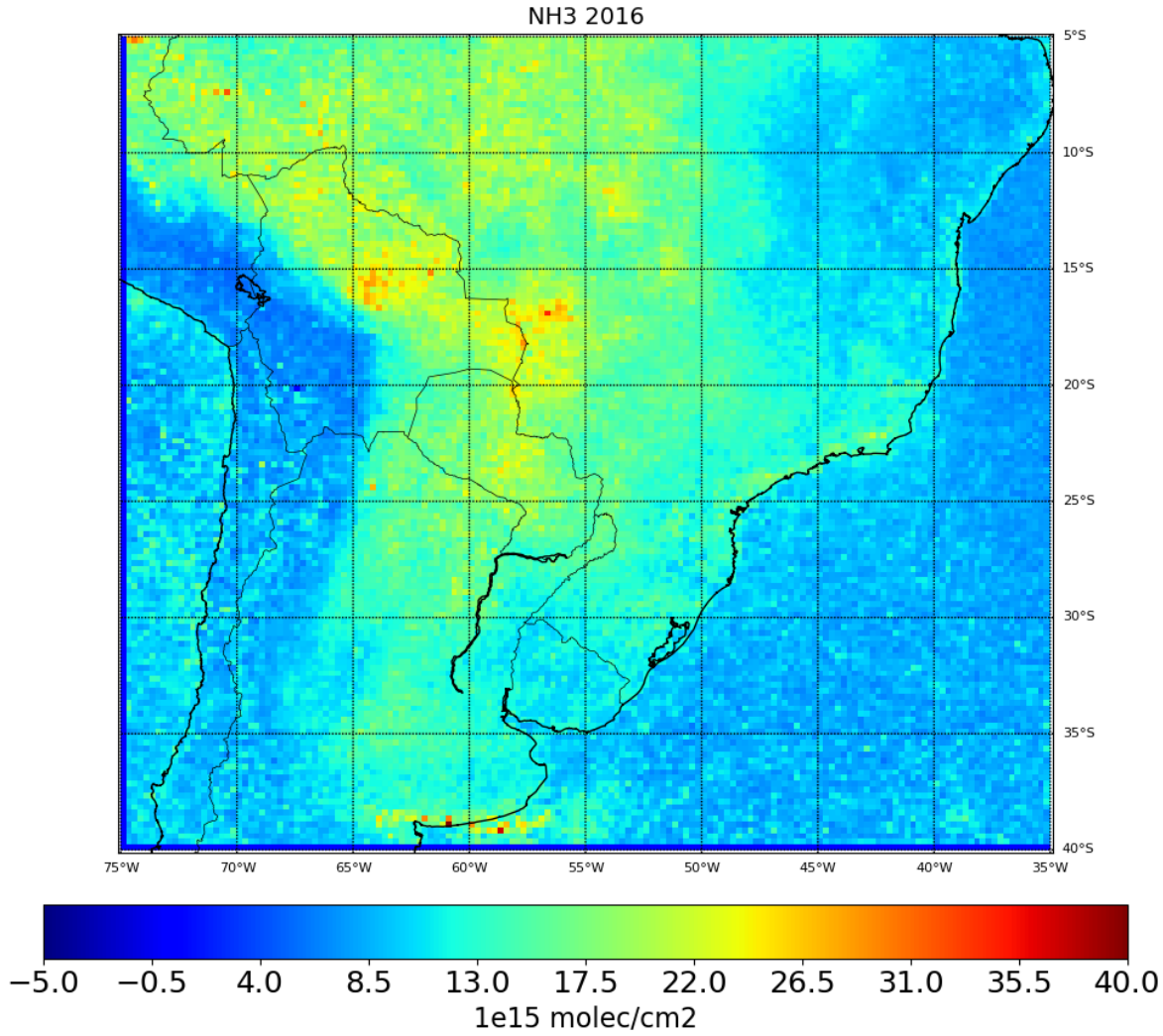

Figure 2.1 *Averaged tropospheric NH_3 columns as observed by the IASI instrument aboard MetOp-A in 2016.*

2.2 DECSO

Daily Emission estimates Constrained from Satellite Observations is a fast inverse modeling algorithm developed by Mijling and van der A (2012) to update daily emissions of short-live gas based on an extended Kalman filter. The algorithm combines simulated trace gas column concentrations from a regional chemical transport model (CTM) with satellite observations. The sensitivity of column concentrations on local and nonlocal emissions is calculated by including a simplified isobaric surface 2-D trajectory analysis. The DECSO algorithm has been applied to NO_2 satellite observations for NO_x emission estimates and been proved that it can well capture both spatial and temporal variations in NOx emissions. We have already implemented DECSO to estimate NO_x emissions for several regions (East Asia, Europe, Middle East, India, South Africa). In this work package, we will apply DECSO to the ANNI-NH3-v2.1R-I retrieval product to estimating NH_3 emissions over South America.

2.3 Development of DECSO for NH_3

We have developed a new version of DECSO for NH_3 by changing several aspects:

a. We first made a new interface to read observations from IASI. The footprint of IASI is a circle at nadir and there is no averaging kernel provided by the ANNI-NH3-v2.1R-I product. To easily compare with the CTM simulations, we re-calculate the footprint of IASI by assuming it is quadrilateral as OMI.
b. The CTM in DECSO has also been updated for NH3 emissions. We use the up-to-date CHIMERE version v2017 instead of v2013. CHIMERE v2017 is supposed to be faster than v2013.
c. The challenge of applying DECSO to a new gas is to obtain the sensitivity of column concentrations on emissions and its associated error covariances. Since the averaging kernel is not provided by the ANNI-NH3-v2.1R-I product, we compare the column concentration simulated by the CTM directly with the retrieval data. We had to remove calculation modules related to averaging kernel.
d. We set up several runs of DECSO with or without assimilation to compare observations with the CTM forecast. We investigated error covariances based on statistics on observation minus forecast analyses.
e. The CTM used in DECSO is performing the modelling till a pressure level of about 500 hPa. For very high mountain ranges this can lead to too small model layers with unrealistic local model results. This can lead to unrealistic emissions over the Andes. Therefore, all data for grid cells with an average altitude above 3500 m has been removed. Figure 2.2 shows the altitude in the region of the emissions.

The adaptations are based on version 5.1 of DECSO as a starting point, which makes this version 5.1-NH3. More information about the various DECSO versions can be found in the appendix.

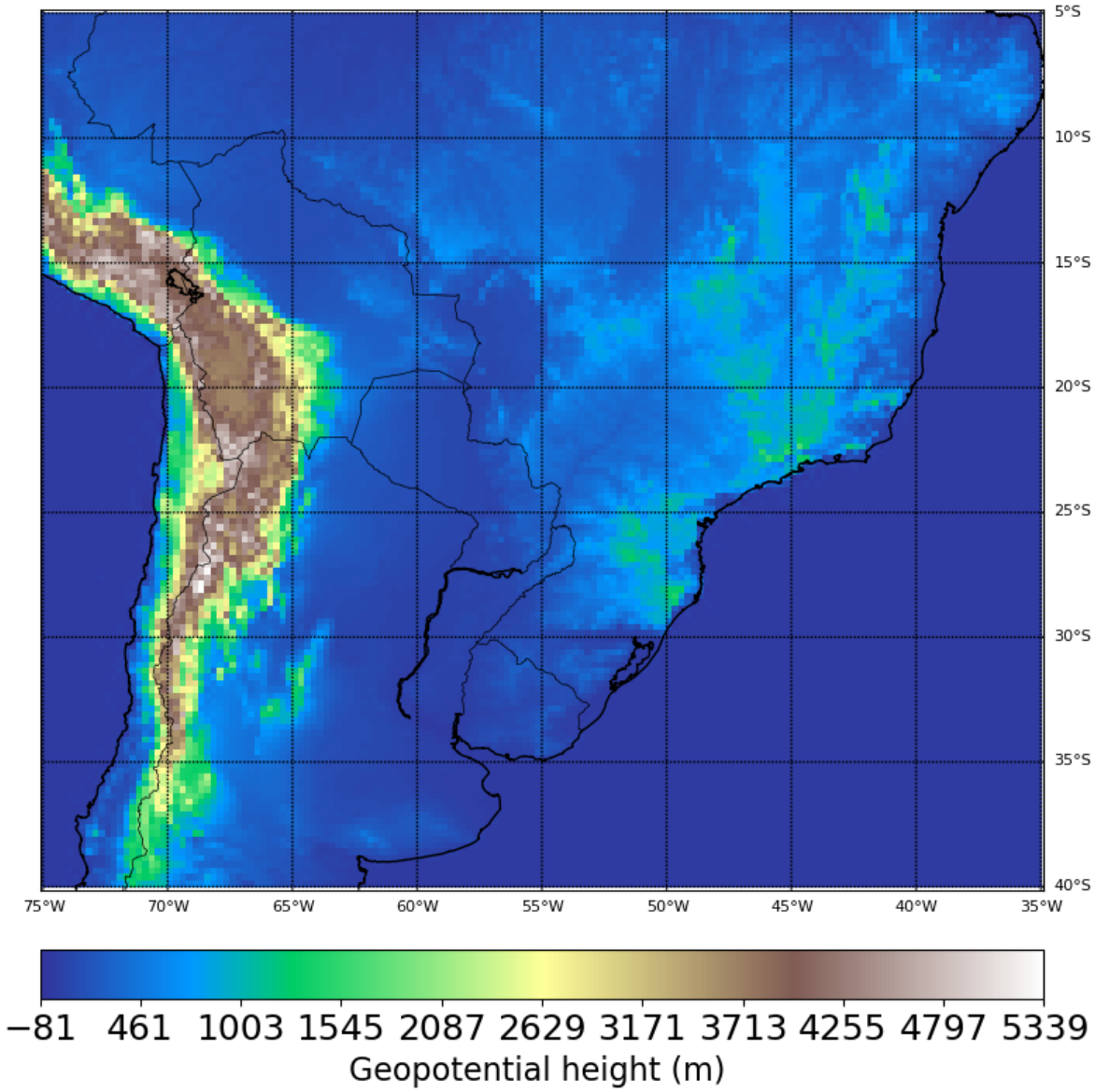

Figure 2.2 *Geopotential height (m) in the region for which the emissions are provided.*

We selected the region from -40º to -5º South and from -75º to -35º West as our study domain. The emissions are calculated with a resolution of 0.25 degree. We use the HTAP 2010 emission inventory as our initial emissions to run the CTM.

2.4 Validation of NH_3 emissions over South America

2.4.1 Comparison to HTAP

We use the HTAP (Hemispheric Transport Atmospheric Pollution) emission inventory version 2 in 2010 as our initial emissions to run the CTM. The spatial resolution of HTAP is 0.1◦ ×0.1◦. HTAP uses nationally reported emissions combined with regional scientific inventories in the format of sector-specific grid maps. The database consists of a combination of gridded regional

emission inventories such as the Model Inter-Comparison Study (MICS) for Asia, Environmental Protection Agency (EPA) for the US and Canada, and the Netherlands Organisation for Applied Scientific Research – Monitoring Atmospheric Composition and Climate (TNO-MACC) II database for Europe. The grid maps are complemented with EDGARv4.3 data for those regions where data are absent.

Figure 2.3 presents the monthly NH_3 emissions from HTAP in 2010. We see NH_3 emissions slightly increase or decrease with the same spatial distribution from month to month. Since the lifetime of NH_3 is very short, about a few hours, we expect the NH_3 emission distribution to be similar to the concentration. The monthly NH_3 column concentrations observed by IASI show different monthly distributions (Figure 2.4). We see a very strong seasonal variation on NH_3 column concentrations in the region. NH_3 column concentrations start to increase in the center of the domain in August. The high NH_3 concentrations are due to biomass burning emissions (van Damme et al., 2018). Figure 2.5 shows the NH_3 monthly emissions derived from satellite observations. We see a clear seasonal cycle from the figure.

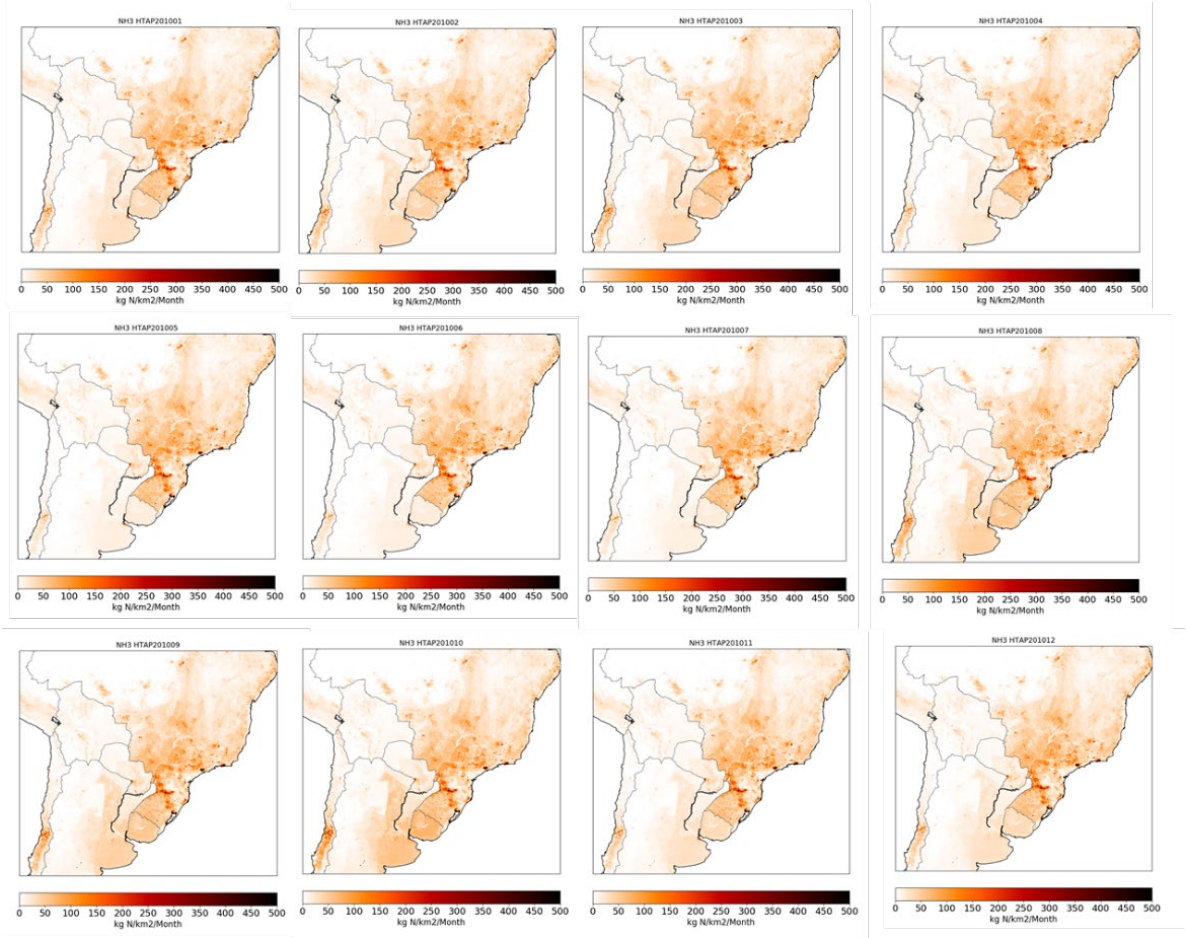

***Figure 2.3**. Monthly NH_3 emissions from HTAP 2010. Data are downloaded from https://edgar.jrc.ec.europa.eu/htap_v2/.*

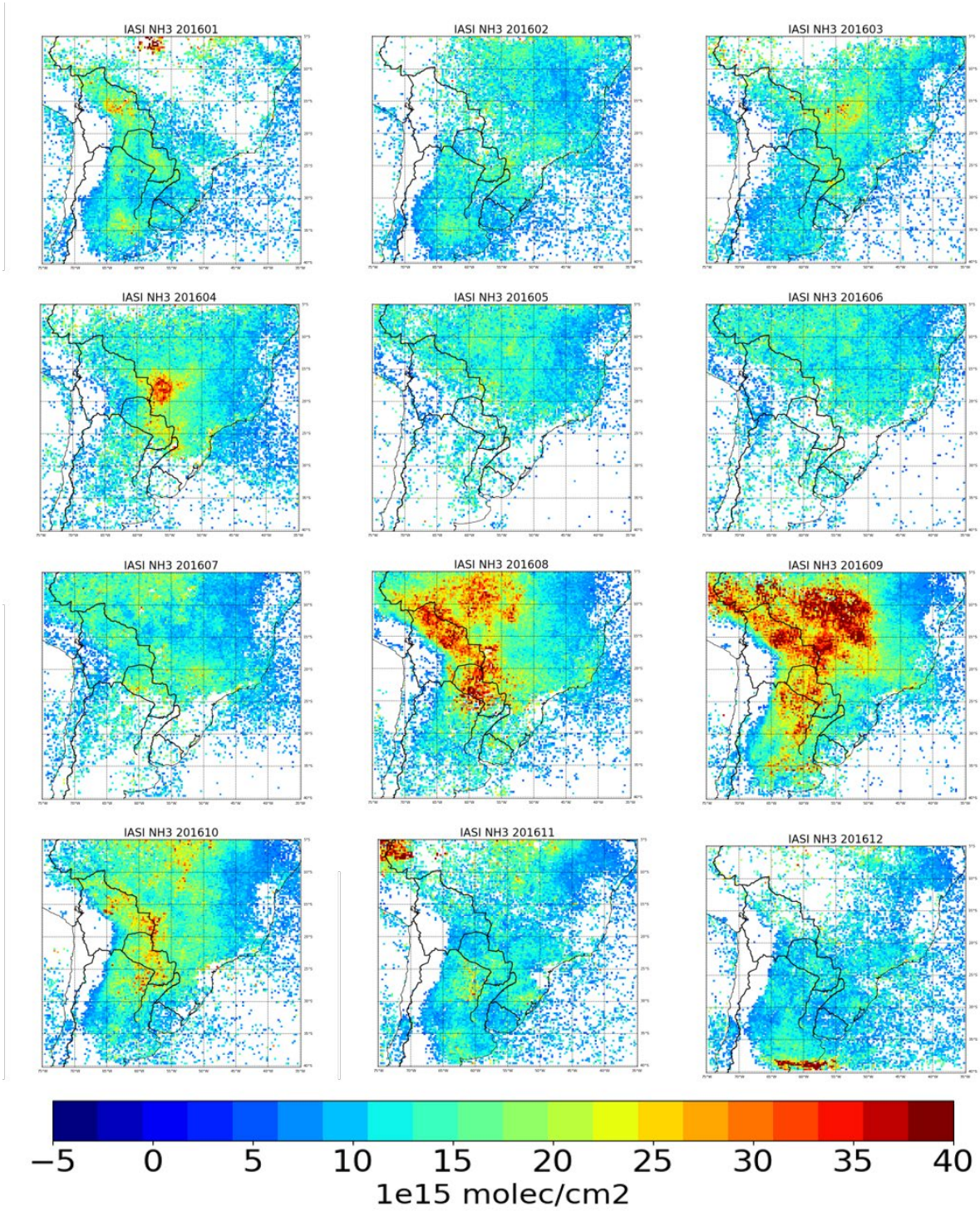

***Figure 2.4**. Monthly tropospheric NH_3 columns in 2016 as observed by the IASI instrument aboard MetOp-A.*

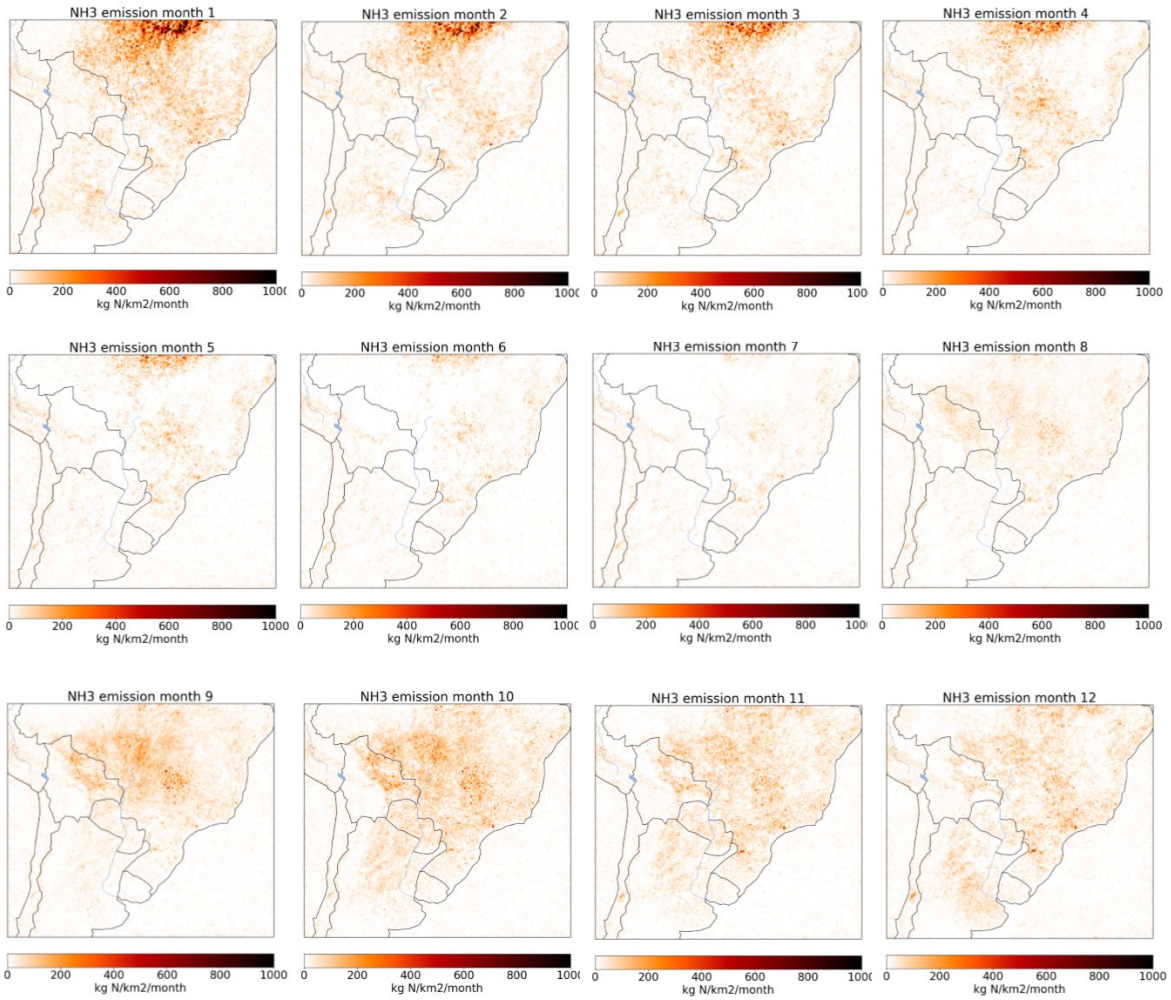

***Figure 2.5**. Monthly NH_3 emissions in 2016 derived with DECSO from IASI observations on MetOp-A.*

2.4.2 Comparison to an Argentinian bottom-up inventory

We have compared the DECSO emissions to an Argentinian bottom-up emission inventory recently published in Puliafito et al. (2020). The bottom-up inventory contains emission for the year 2014 and 2016. We have resampled the 2016 NH_3 emissions to the same grid as DECSO for comparison. Figure 2.7 shows the comparison between the annual bottom-up and the annual averaged NH_3 emissions of DECSO. The bottom-up inventory of Argentina shows that NH_3 emissions are mainly distributed in the east part of Argentina (see Figure 2.6). Two strong point sources are shown in the city area of Buenos Aires and Concepción del Uruguay. However, these two strong points are not seen from satellite observations and also not found in the point source emission study from Dammer et al. (2019) and van Damme et al. (2018). Figure 2.6 shows that NH_3 emissions estimated with DECSO from IASI on MetOp-A are mainly distributed over cropland and herbaceous areas (see the land use map of Figure 2.7).

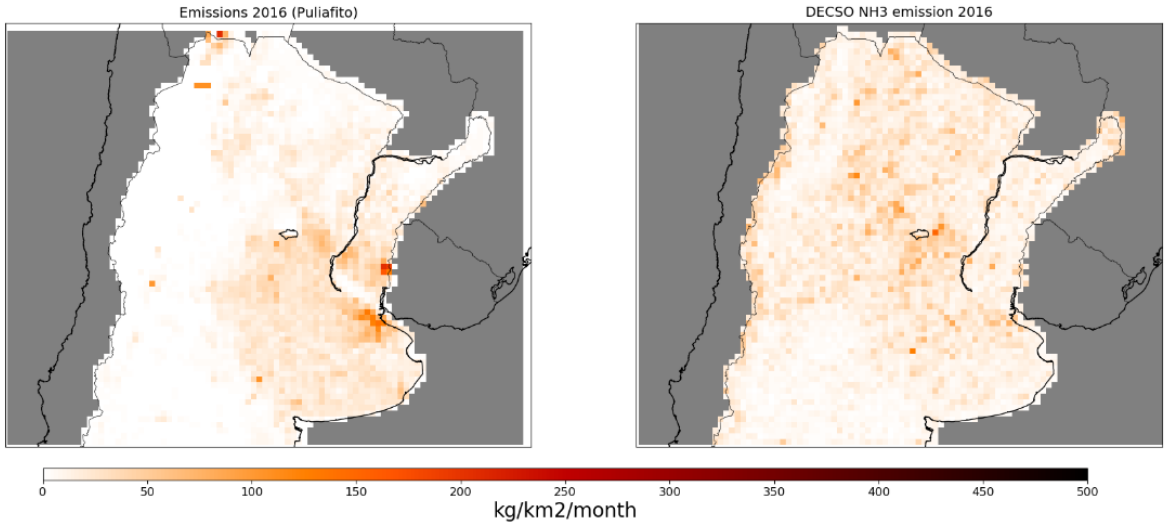

Figure 2.6 *Comparison of the NH_3 emissions over Argentina from the bottom-up inventory in 2016 (left plot) and the DECSO emissions in 2016 (right plot).*

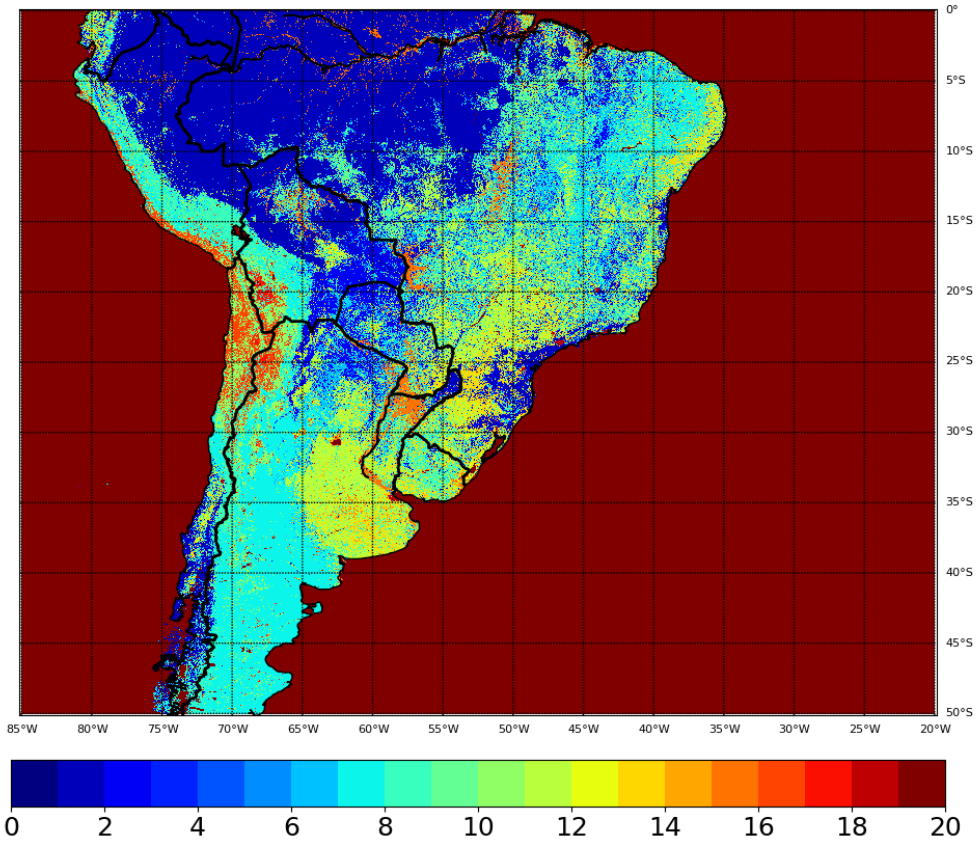

Figure 2.7. *Landuse map in South America in 2013. The number represents different landuse categories. 1.Broadleaf Evergreen Forest; 2.Broadleaf Deciduous Forest; 3.Needleleaf Evergreen Forest; 4.Needleleaf Deciduous Forest; 5.Mixed Forest; 6.Tree Open; 7.Shrub; 8.Herbaceous; 9.Herbaceous with Sparse Tree/Shrub; 10.Sparse vegetation; 11.Cropland; 12.Paddy field; 13.Cropland / Other Vegetation Mosaic; 14.Mangrove; 15.Wetland; 16. Bare area, consolidated (gravel, rock); 17. Bare area, unconsolidated (sand); 18.Urban; 19. Snow / Ice; 20. Water bodies. The landuse dataset is the product version 3 from the Global Land Cover by National Mapping Organizations (GLCNMO). The data were prepared by using MODIS data with remote sensing technology. More information about the data can be found on https://globalmaps.github.io/glcnmo.html*

3 Hydrocarbon fluxes constrained by OMI and TROPOMI (WP3)

3.1 HCHO observations from OMI and from TROPOMI

We make use of HCHO observations from OMI for the period 2005 to 2017 and from TROPOMI for May 2018 to December 2018. The OMI QA4ECV product (http://www.qa4ecv.eu) shows fewer negative columns related to clouds, and reduced noise compared to previous products over this region, as detailed in De Smedt et al. (2018). The issues related to the row anomaly have been accounted for and the recommendations for the quality flag have been followed. This led to a good data quality with increased signal-to-noise ratio. The operational TROPOMI product (http://scihub.copernicus.eu) is used, but is modified to account for improvements in the background correction, destriping and recommendation on quality flags**.** For both products, we build monthly averages at the model resolution (0.5°x0.5°).

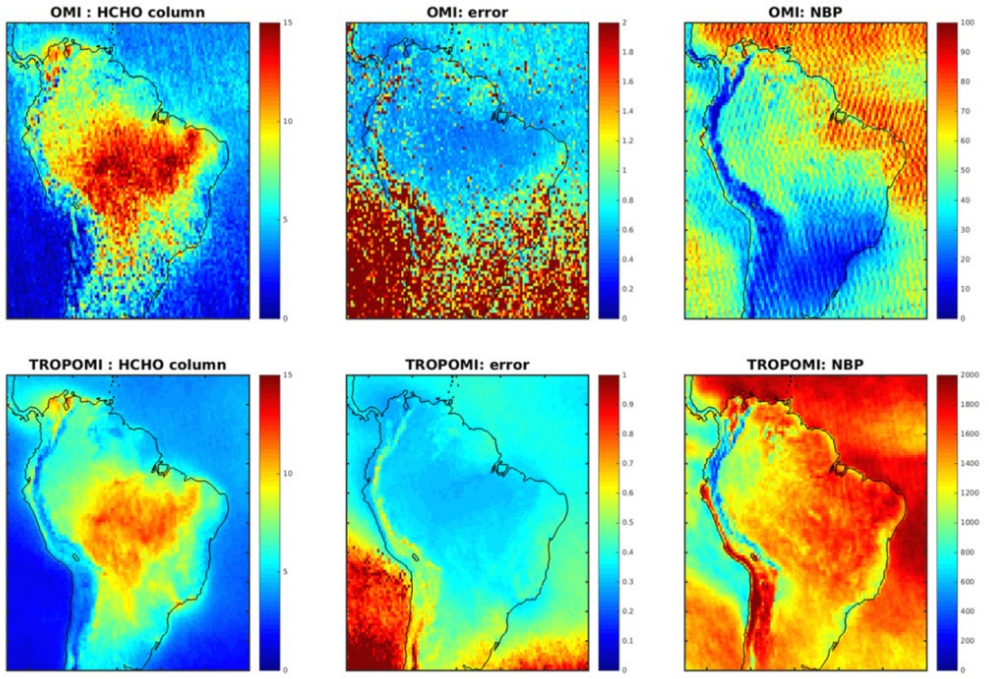

Figure 3.1*: HCHO columns measurements (left, in 10^{15} molec.cm^{-2}), relative uncertainty (middle) and number of measurements per pixel (right) for OMI (upper row) and TROPOMI (lower row) for May to December 2018. Note the different color-scale highlighting the lower uncertainty (x2) and the higher number of measurements per grid cell (x20) of TROPOMI compared to OMI.*

The left panels of Figure 3.1 show the average HCHO column (in 10^{15} molec.cm^{-2}) for OMI and TROPOMI for the same period (May to December 2018). The middle panels show the relative uncertainty on the retrievals, and the right panels the number of measurements per pixel per month. Note the higher uncertainty and fewer measurements over the southern part of South America and over the Andes for OMI, compared to TROPOMI. We also observed a slight decline in the number of measurements for OMI with a trend of about -1% yr^{-1} over

most parts of the region, but with stronger decline (about -3% yr^{-1}) over the Andes and over the most southern part of the region below 20°S (not shown).

3.2 Bias correction of the satellite datasets

A recent validation study, based on a comparison of TROPOMI HCHO data in 2018 and FTIR column measurements at 25 stations worldwide, reported biases in the TROPOMI data that were dependent on the HCHO concentration levels (Vigouroux et al., 2020). They found that TROPOMI overestimates very low levels of HCHO (<$2.5 \cdot 10^{15}$ molec.cm^{-2}) by +26%(±5), and underestimates high HCHO (>$8 \cdot 10^{15}$ molec.cm^{-2}) levels by -30%(±1.4). However, this study was based on a limited amount of data in Southern America obtained in 2018 and does not provide a bias correction for the OMI dataset. For the purposes of the SOLFEO project, we have derived a bias-correction for the OMI and TROPOMI datasets as follows.

- Firstly, we found that inconsistencies between different cloud products led to large differences between OMI and TROPOMI HCHO. The mismatch was strongly decreased when OMI and TROPOMI clear-sky air mass factor data were used.
- Secondly, we performed a linear regression between monthly averaged FTIR observations at Paramaribo (Surinam, 2005-2017) and at Porto Velho (central Brazil, 2016-2017), and the OMI observations at the same months and locations.
- Finally, we performed a linear regression between the TROPOMI and OMI columns based on monthly averaged data over land between May and December 2018. Only satellite data with relative uncertainty lower than 100% were considered.

These steps are illustrated in Figure 3.2. The resulting bias-corrections for OMI and TROPOMI clear-sky air mass factor data are expressed as 1.236·OMI-0.83 and 1.358·TROPOMI-0.83, respectively, as shown in Figure 3.2.

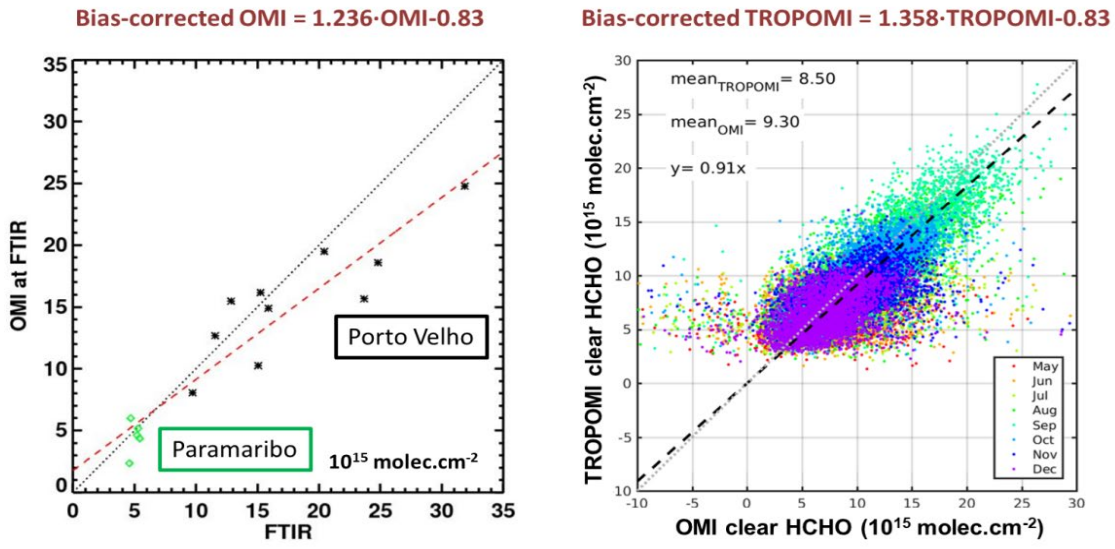

***Figure 3.2**: Linear regression (left) between the OMI clear-sky air mass factor data and FTIR column observations at Paramaribo and Porto Velho and (right) between OMI and TROPOMI clear-sky air mass factor data over May-December 2018. The bias-corrected satellite datasets will be used in the MAGRITTE model as top-down constraints for the inversion.*

3.3 The MAGRITTE model and the inversion method

The space-based emission estimates are derived by an iterative minimization algorithm based on the full adjoint of the regional chemical transport model MAGRITTE (Model of Atmospheric composition at Global and Regional scales using Inversion Techniques for Trace gas Emissions, Müller et al., 2019). The boundary conditions of the regional model at the lateral borders come from the global IMAGES model (Bauwens et al., 2016; Müller et al., 2019; Stavrakou et al., 2016).

MAGRITTE calculates the concentrations of more than 170 transported chemical constituents at 0.5°x0.5° horizontal resolution and 40 vertical levels between the surface and the lower stratosphere. The chemical oxidation mechanism for isoprene is based on Stavrakou et al. (2010), but is modified to account for the kinetics of isoprene peroxy radicals (Peeters et al., 2014). Based on box model simulations, the formaldehyde yield in isoprene oxidation by OH is calculated to be 1.9 mol mol^{-1} at low NOx conditions prevalent in the Amazon forest.

Meteorological fields are obtained from ECMWF ERA-Interim reanalysis. The model uses a priori biogenic emissions from the MEGAN-MOHYCAN model (Stavrakou et al., 2014), a priori emissions for open vegetation fires from GFED4s (Werf et al., 2017) and a priori anthropogenic emissions in South America from EDGAR4.2 (http://edgar.jrc.ec.europa.eu).

The mismatch between the CTM and the observations is minimized through an iterative quasi-Newton optimization algorithm (Müller and Stavrakou, 2005). Monthly emissions are derived on the global scale at the resolution of the model (0.5°×0.5°). The inversions are carried out separately for all years of the period 2005 to 2017 for OMI and May to December 2018 for TROPOMI. The errors in the satellite data used in the inversion system are calculated as the squared sum of the retrieval error and a representatively error set to 2×10^{15} molec.cm^{-2}. The assumed error in the a priori biogenic fluxes is factor of 3. About 20-30 iterations are generally required to reach convergence.

3.4 OMI-based emissions and emission trends (2005-2017)

The bias-corrected OMI columns, the a priori model columns and the HCHO columns after inversion are displayed in Figure 3.3 and Figure 3.4. Overall, the a priori columns are by about 20% higher than OMI columns on average, and a similar bias is observed during the different seasons. However, there exist large differences across the regions, with strong positive a priori bias over the Amazon rainforest (+20%) and a very good a priori agreement over the open savanna (1%), as displayed in Figure 3.3. The mismatch between the model and the observed columns is substantially reduced after inversion, both in terms of absolute magnitude and correlation (Figure 3.3 and Figure 3.4).

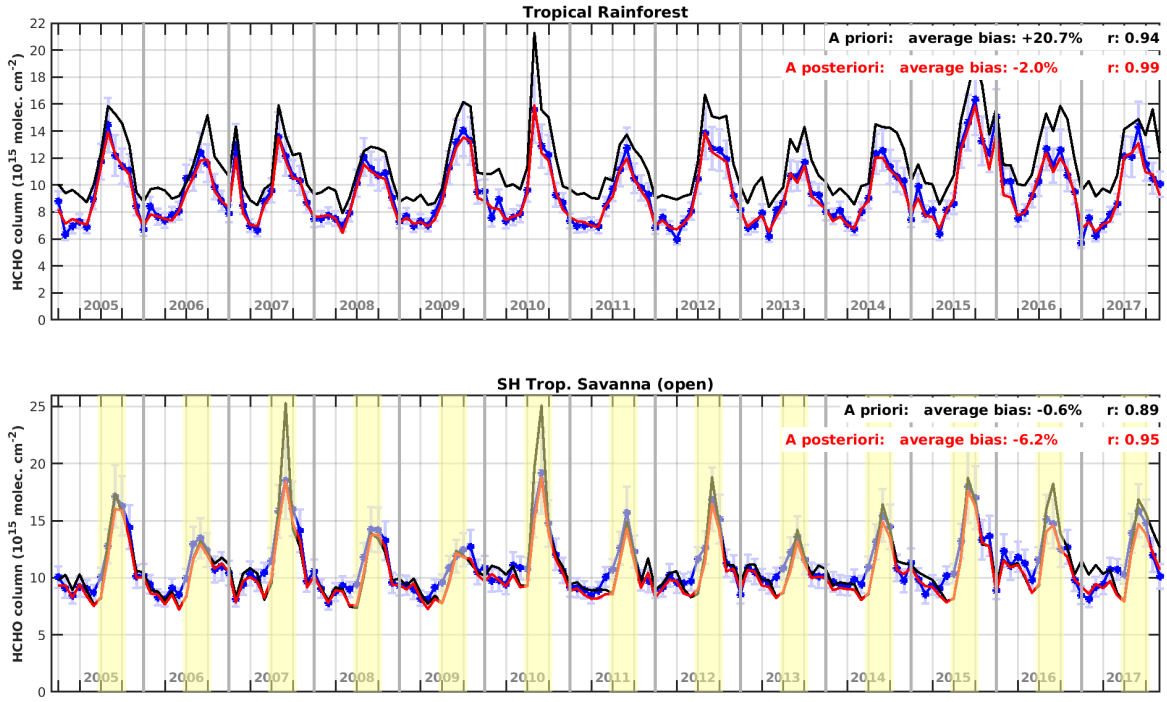

***Figure 3.3**: Observed (blue), a priori (black) and a posteriori (red) HCHO columns over 2 regions, the tropical rainforest (5°S-1°N, 60-75°W) and Southern Hemisphere tropical savanna (5-18°S , 44-52°W). The yellow shaded areas indicate the fire season.*

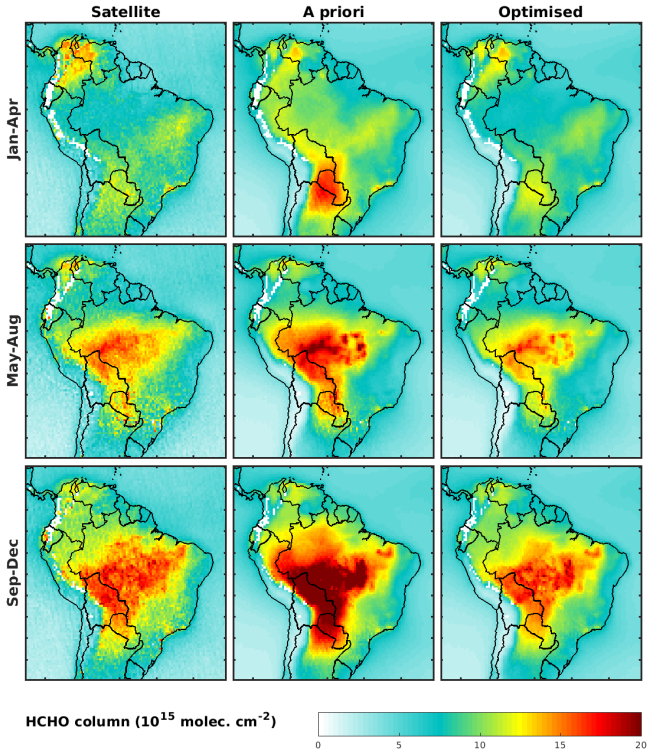

***Figure 3.4**: HCHO columns over South America during the wet season (January-April), the wet-to dry transition (May-August) and the dry season (September-December), averaged over 2005-2017. The bias-corrected OMI columns, the a priori MAGRITTE columns and the inversion results are shown on the left, middle and right panels, respectively.*

The a priori and a posteriori emission estimates and the emission increments are illustrated in Figure 3.5. On average over the total domain, the OMI observations suggest an annual reduction of the isoprene emissions by 26%, and significant changes in the spatial emission distribution.

Compared to the a priori emissions, we find lower isoprene fluxes over the high-emitting Amazon rainforest, whereas higher isoprene fluxes are inferred in the open savanna. The strong decrease over the forest likely indicates that isoprene flux capacities for tropical forests might be overestimated in MEGAN. The emission increase suggested over the Andes, and the strongly decreased emissions over Paraguay are more uncertain given the lower column abundancy and higher uncertainty of the HCHO retrieval in these regions (see section 3.1).

Fire emissions in South America exhibit a large interannual variability. The inversion of OMI data suggests a less pronounced variability with stronger flux decreases during years with intense fire activity (33% decrease in 2010), compared to years with fewer fires where a moderate reduction is suggested by the inversion (e.g. from 10.1 to 9.1 Tg/year in 2008). On average, the fire emissions are reduced by 20% for the total region. As can be seen in Figure 3.5 the strongest reduction is suggested in the in the central part of Brazil where the biggest fires occurred in 2010.

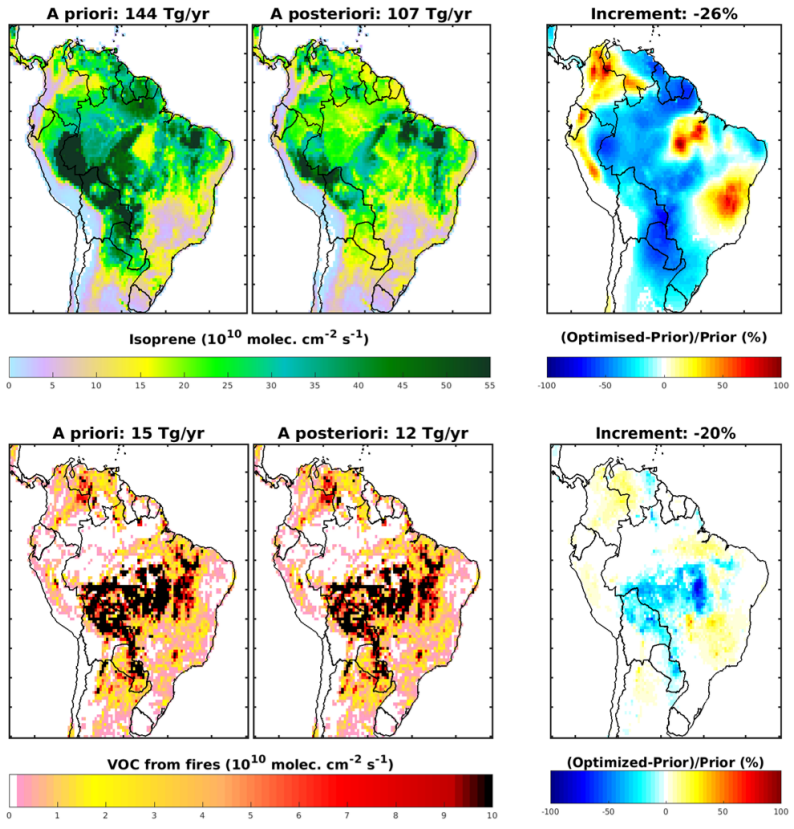

***Figure 3.5**: Average annual emissions for isoprene and for pyrogenic VOCs for 2005-2017. A priori and OMI-based emissions are given and the increment map, showing where emission changes are suggested by the inversion.*

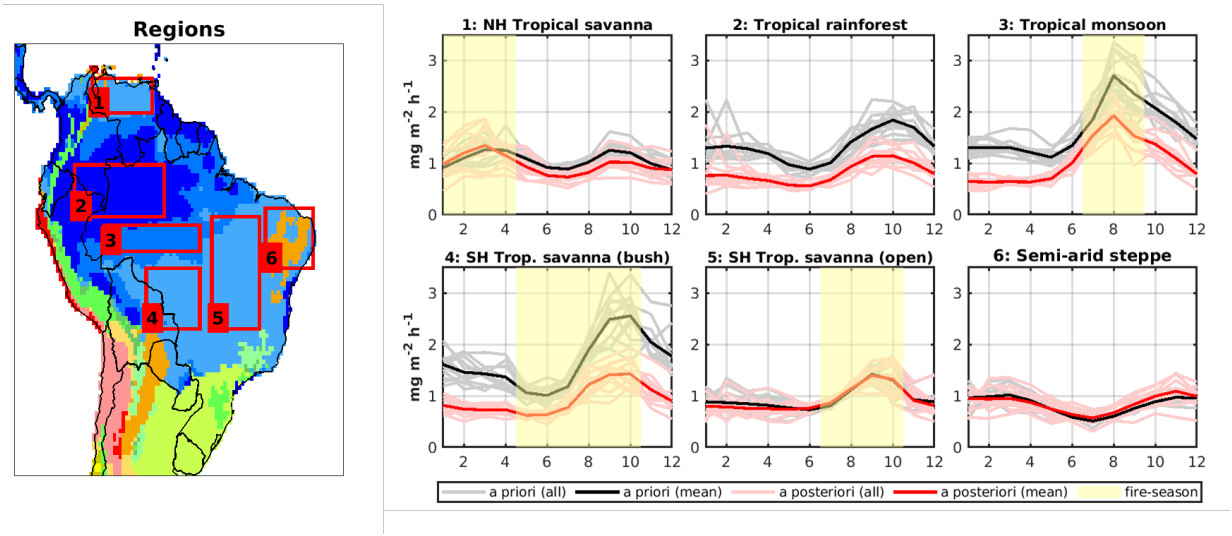

***Figure 3.6**: The seasonal pattern of a priori isoprene emission estimates (black) and OMI-based estimates (red) for 6 regions chosen based on the Köppen-Geiger climate classification map shown in the left panel. The dark lines show the average seasonal pattern for the period 2005-2017, the light lines show the monthly fluxes for the individual years.*

Figure 3.6 illustrates the impact of the inversion on the seasonal pattern of the isoprene emissions. In the northern hemisphere tropical savanna (region 1), the inversion does not suggest large changes, although a slight reduction is found during the wet season. For the woody vegetation types in the amazon forest (regions 2-3), the inversion suggests an all-year round decrease. In the southern hemisphere tropical savannah (region 4), a stronger reduction is suggested by the end of the dry season, resulting in a reduced amplitude of the seasonal cycle (peak-to-trough = factor of 2.5 in the a priori, 2 in the a posteriori). Very little changes are inferred over the tropical open savanna and in the semi-arid steppe. Overall, for all regions, the seasonal patterns is not much affected by the inversion.

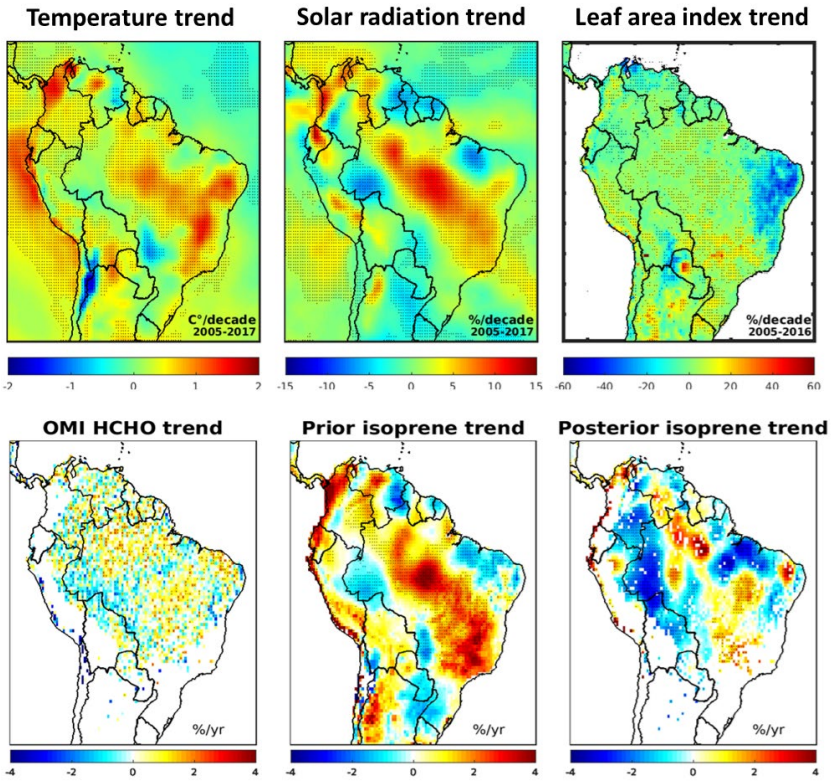

***Figure 3.7**: Maps showing the annual trends for the period 2005-2017.*

The upper panels show the trends for the temperature, the solar radiation and the leaf area index, being three driving parameters in the MEGAN MOHYCAN model used to calculate the a priori emission estimates.

The lower panels show the trend for the OMI HCHO columns, the a priori and the a posteriori isoprene emission estimates

Figure 3.7 depicts the trends of OMI-based isoprene emissions over 2005-2017. The inversion suggests important changes in the emission trends. The a priori trends (ranging between -2%/yr and +4%/yr) are positive in most regions, mainly driven by the positive trends in temperature and in solar radiation. But the negative HCHO trends found in many regions (lower left panel in Figure 3.7) bring the a posteriori isoprene emission trends to less positive, and even frequently negative values in many regions (ranging between -4%/yr and +3%/yr).

In Figure 3.8 we examine the possible role of deforestation trends derived from satellite Landsat forest cover data at 30 m resolution (Hansen et al., 2013, 2020). In that study, forest loss is defined as disturbance or complete removal of tree cover canopy. Any conversion of natural forests to e.g. plantations, selective logging or shifting cultivation practiced by local communities is also considered as forest loss. According to forest loss and gain data for South America, deforestation occurs over most of Brazil and Northern South American countries, whereas it is negligible in the central and northern parts of the tropical rainforest. We find strong forest loss in Brazilian Para and Mato Grosso regions, and in Paraguay. In Figure 3.8, the decline of tree cover is compared with the annual isoprene emission trends over these regions. Clearly, the strong deforestation rates in those regions are partly responsible for the discrepancy between the a priori and a posteriori emission trends.

However, although about half of the isoprene trend difference can be attributed to forest loss over regions subject to strong deforestation, this is not the case when analyzing a larger region such as Amazonia (15°S to 1°N and 75°W to 43°W), for which the forest loss trend is lower (-0.32% yr-1), even though the isoprene trend difference remains strong (-1.21% yr^{-1}).

We conclude that deforestation alone cannot account for the strong negative a posteriori trend. Isoprene flux inhibition as result of rising CO_2 could explain a decrease in isoprene flux of

~6% over 2005-2017. To fully understand the trend in isoprene emissions, the development of bottom-up inventories accounting for land cover changes and CO_2 inhibition in models will be needed. Note also that, the meteorological trends from ERA-Interim analyses currently used as input to calculate the a priori isoprene emissions are very uncertain in these regions. Therefore, the overall positive trend of a priori emissions derived in our study should also be re-evaluated in future by the use of the ERA5 analysis, and possibly other datasets such as GFS and MERRA.

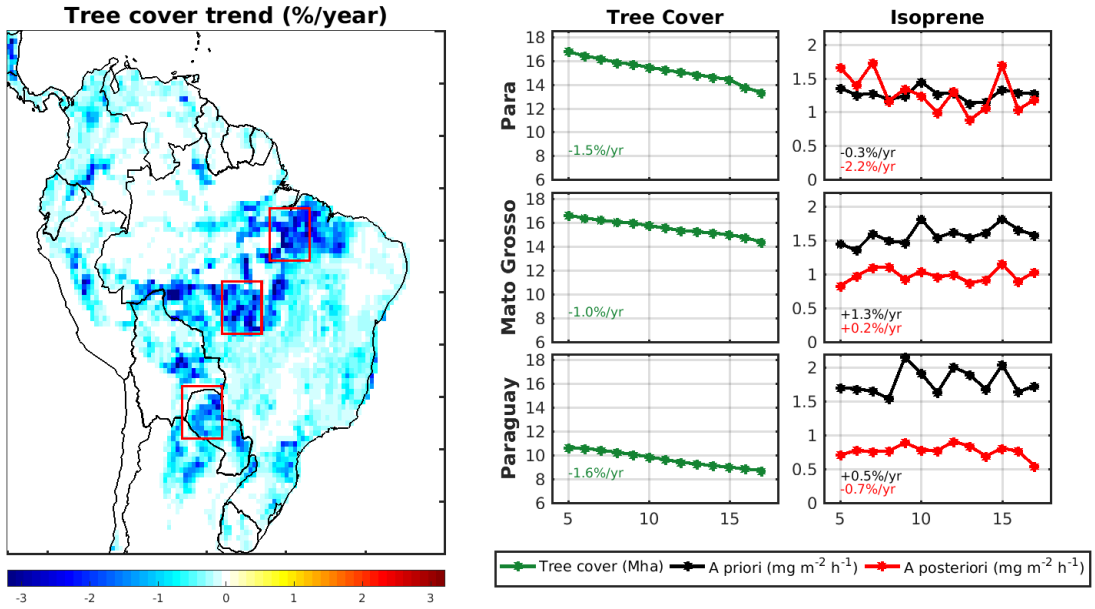

***Figure 3.8**: Left: Trend map showing the annual tree cover trend in %/year over South America. The red rectangles indicate the three regions for which time series and shown in the right panels of the figure. Right: In green, the total tree cover per regions is shown, the a priori (black) and a posteriori (red) isoprene fluxes are shown for the same regions. The annual trend for each parameter in given in the left corner of each plot.*

3.5 Inversions based on TROPOMI (May-December 2018)

We conducted an inversion of VOC fluxes for 2018 constrained by the bias-corrected TROPOMI HCHO (see section 3.2) over May-December. The model uses a priori fire emissions from GFED4s and biogenic emissions from the MEGAN-MOHYCAN inventory for the same year. On annual basis, the satellite data suggest a reduction of the a priori isoprene emissions, by about 30% (from 137 to 97 Tg, Figure 3.9). Important changes in the spatial patterns are suggested, with emission reductions of up to 60% over the Amazon rainforest and emission increases of up to 50% over the Brazilian highlands. The changes in the spatial pattern are very similar to the results obtained with the inversion based on OMI shown in Figure 3.5. Furthermore, the TROPOMI data infer a moderate decrease in biomass burning emissions, from 9 to 7 TgVOC for 2018. This decrease is comparable to the OMI-based emission estimates for years with moderate fire activity (like 2018).

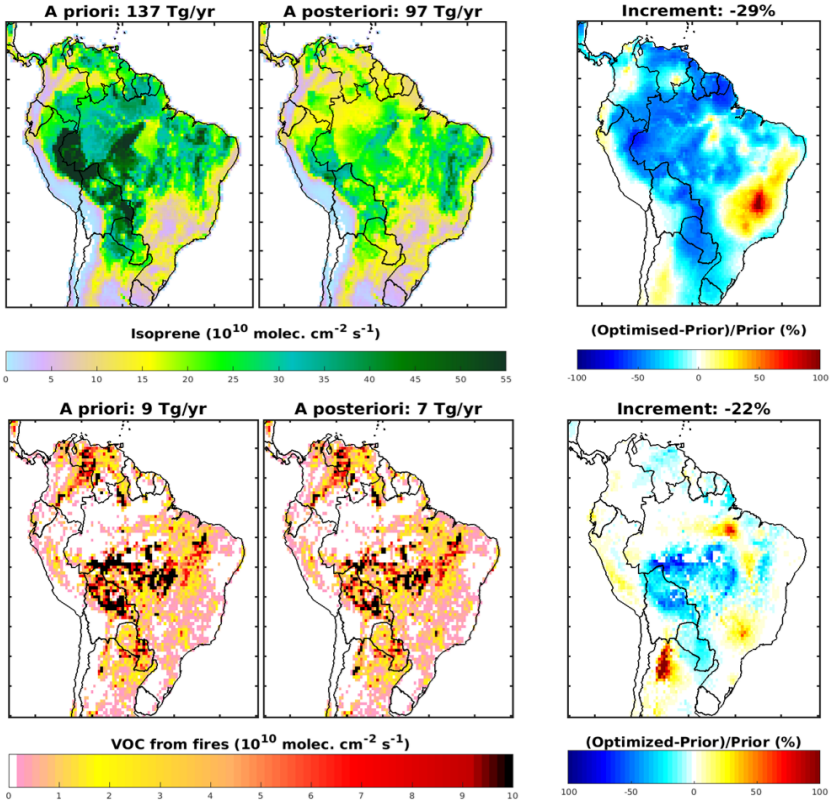

***Figure 3.9**: Annual emissions of isoprene and pyrogenic VOCs for 2018. A priori and TROPOMI-based emissions are shown as well as the increment distributions suggested by the inversion.*

3.6 Sensitivity tests to estimate uncertainty

In order to evaluate the sensitivity of the inferred emission estimates to some of the key uncertainties in the model and in the satellite data, we conducted five sensitivity experiments, briefly described in Table 1. The sensitivity inversions S1 addresses the large uncertainties in the emissions of other hydrocarbons contributing to HCHO formation, like methanol and monoterpenes. Past studies based on satellite observations suggested that the methanol sources from the MEGAN inventory (used as a priori in the model) might be strongly overestimated over South America (Stavrakou et al., 2011; Wells et al. 2014). Therefore, we assumed a source of methanol and monoterpenes twice lower than in the a priori in the sensitivity inversion S1.

Another major area of uncertainty relates to the emissions of NO from soils. In situ data, although sparse in this region, and satellite observations indicate a large underprediction of current state-of-science modelled NO_2 concentrations, most likely due to underestimated soil NO emissions. The sensitivity experiment S2 addresses this uncertainty. The higher soil NO emissions affect NOx and therefore OH levels, thereby modifying the HCHO production yields from hydrocarbons.

In S3, we replace the MODIS-based aerosol optical depth (AOD) climatology by assimilated AOD provided by the CAMS model. In this way, we account for a source of uncertainty, particularly important during fire episodes. Finally, in S4 and S5 we account for uncertainties in the TROPOMI bias correction relationship of the standard inversion (1.358×TROPOMI-0.83), as shown in Table 3.

Table 3. Description of the different sensitivity inversions performed in 2018.

Name	Description
STD	Standard inversion using TROPOMI HCHO clear-sky AMF, corrected for biases (1.358·TROPOMI-0.83), excluding data where surface altitude is above 1 km
S1	As STD, emissions of methanol and monoterpenes halved
S2	As STD, soil NO emissions multiplied by 3
S3	As STD, aerosol optical depth from the CAMS model
S4	As STD, lower HCHO columns to account for uncertainties of the bias correction in TROPOMI data (1.211·TROPOMI-0.83)
S5	As STD, higher HCHO columns to account for uncertainties of the bias correction in TROPOMI data (1.505·TROPOMI-0.83)

Table 4 provides the average observed and modelled HCHO column over the studied domain for the standard inversion and for each of the five sensitivity experiments. Notice that the inversions STD, S1, S2 and S3 are constrained by the same satellite data (annually averaged column of 9.6×10^{15} molec.cm^{-2} over the model domain) whereas S4 and S5 are constrained by TROPOMI columns, which are by 12% lower or higher, respectively. The average a priori modelled HCHO column varies between 10.0×10^{15} (when lower emissions of methanol and terpenes are assumed) and 11.3×10^{15} molec.cm^{2} (when soil NO fluxes are tripled). After inversion, a very good overall match with the observations is achieved, with a bias of less than 5% relative to the satellite observations, except in the case of inversion S5 for which the a posteriori bias is slightly increased.

	HCHO column (10^{15} molec.cm^{-2})		
	TROPOMI	**A priori**	**Optimized**
STD	9.6	10.5 (+9%)	9.3 (-4%)
S1	9.6	10.0 (+4%)	9.2 (-4%)
S2	9.6	11.3 (+18%)	9.5 (-1%)
S3	9.6	10.4 (+8%)	9.3 (-4%)
S4	8.5	10.5 (+23%)	8.5 (0%)
S5	10.8	10.5 (-3%)	10.1 (-6%)

Table 4. Average HCHO column (in 10^{15} molec.cm^{-2}) over the studied domain as observed by TROPOMI (bias corrected), and modelled before and after inversion. The bias with respect to the observations is given in parentheses. Note that oceanic data are not considered.

Figure 3.10 illustrates the spatial distribution of the a priori isoprene emission estimates and the a posteriori estimates, as well as the percentage difference maps for all sensitivity runs. On average, the total isoprene emissions are reduced by 14 to 44% with respect to the a priori resulting in total isoprene emissions of 77 to 117 Tg. The difference maps indicate that in all cases the inversion suggests similar changes in the spatial pattern of the isoprene emissions, namely lower isoprene emissions over the Amazon forest (of up to 80%), and higher isoprene emissions over the Brazilian highlands (50-100%).

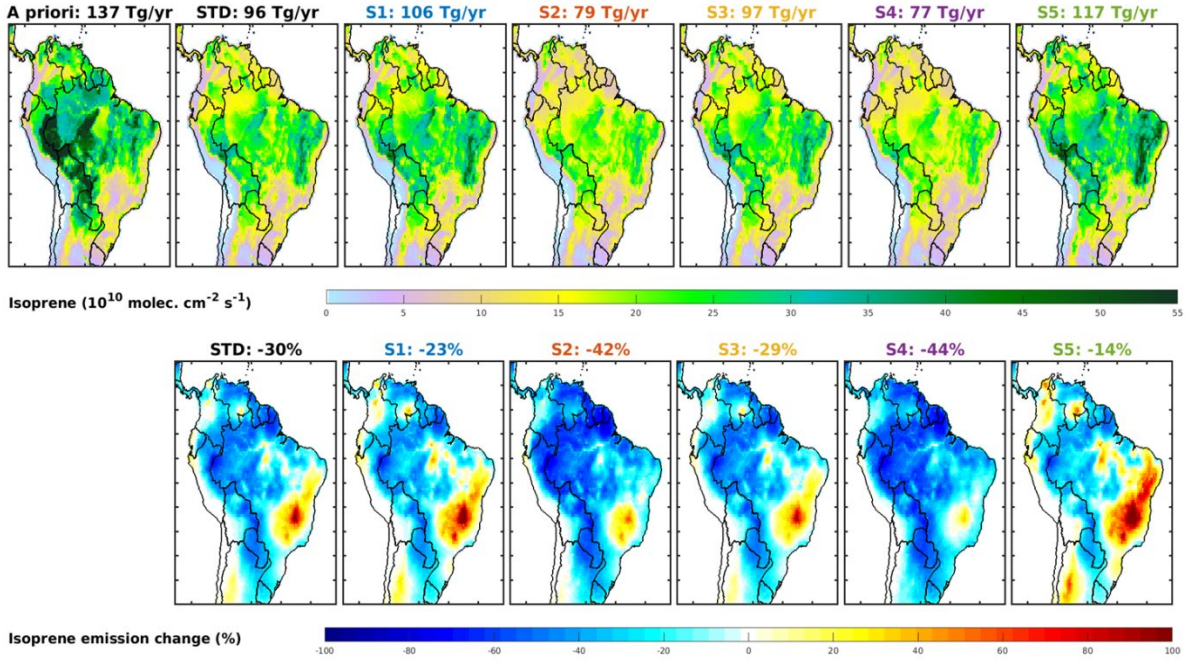

***Figure 3.10**: Upper panel: Spatial distribution of a priori isoprene emissions as well as of a posteriori estimates for all sensitivity runs. Lower panels: Spatial relative difference induced by the inversion with respect to the a priori.*

Figure 3.11 illustrates the seasonal pattern inferred by the inversion for all sensitivity runs. All experiments agree on the seasonal patterns. For the regions 1-4, all inversions agree on an all year-round emission decrease. This result underlines the robustness of the emission estimates in these regions. In the open savannah and the semi-arid steppe (regions 5 and 6), the a priori estimates lie within the variability of the inversion results, pointing out the more uncertain emission estimates in these regions. Note that the overall changes in the seasonal patterns are well in line with the changes suggested by the OMI-based inversions shown in Figure 3.6.

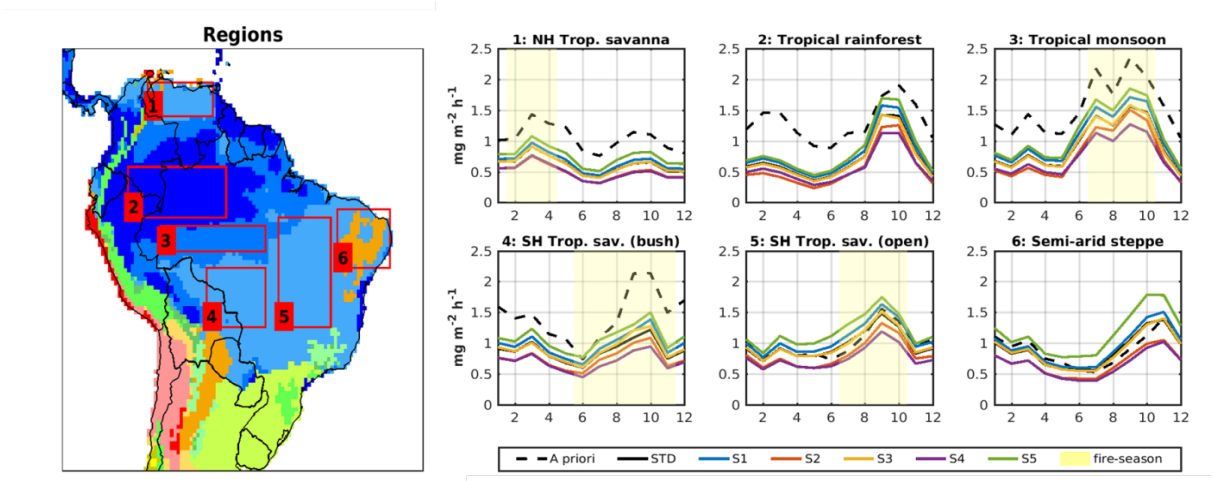

***Figure 3.11**: Seasonality of a priori and top-down isoprene emissions for all sensitivity runs (Table 1) for six regions chosen based on the Köppen-Geiger climate classification map shown on the left.*

Figure 3.12 illustrates the spatial distribution of the a priori and top-down fire VOC emission estimates, and the difference maps for all sensitivity experiments. On average, the fire VOC emissions are reduced by 17 to 24% with respect to the a priori, resulting in total fire VOC emissions of 6.7 Tg to 7.4 Tg. Overall the spatial pattern is not much affected by the inversion with a maximal reduction of 60% in southern Amazon rainforest and woody savannas. Note also that inferred changes in the spatial pattern are very similar for all sensitivity runs underlining the robustness of the inversion for fire emissions.

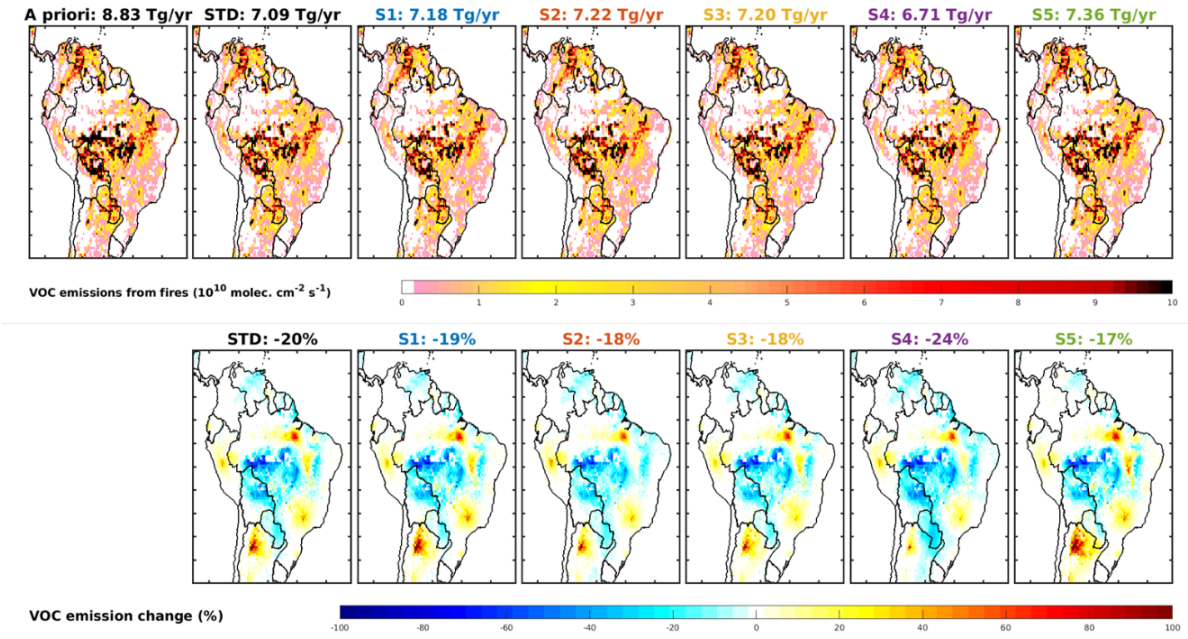

***Figure 3.12**: Upper panels: A priori and top-down fire VOC emission estimates for all sensitivity runs (see Table 1). Lower panels: Relative difference induced by the inversion with respect to the a priori.*

4 Soil and anthropogenic NOx emissions using TROPOMI (WP4)

4.1 Development of the NO_x emission algorithm

DECSO algorithm

The DECSO algorithm (Mijling and Van der A, 2012) is specifically designed to use daily satellite observations of column concentrations for fast updates of emission estimates of short-lived atmospheric constituents on a mesoscopic scale (0.25°×0.25°). An extensive description of the algorithm can be found in the GlobEmission ATBD (van der A et al., 2016). We use the DECSO algorithm together with the regional CTM CHIMERE (Schmidt et al, 2001; Bessagnet et al., 2004) on a 0.25° resolution, driven by operational meteorological forecast of the European Centre for Medium-Range Weather Forecasts (ECWMF). The CTM implementation is described in more detail by Mijling et al. (2009). We have used NO_2 observations from the OMI or the GOME-2 instrument, but for this project we have switched to the high resolution observations of TROPOMI on Sentinel 5p. This data is available through the Copernicus Sentinel data hub and the TEMIS portal (http://www.temis.nl). NO_2 retrievals at cloud fractions larger than 20% are filtered out to reduce the influence of the modelled NO_2 column below the clouds. Retrievals with low clouds (below 800 hPa) are also rejected because the intersection of the cloud with the NO_x bulk makes the retrieval too sensitive for the exact cloud height. Before comparing the model simulations with the satellite observations, the CHIMERE vertical profiles are extended from the model ceiling (at 500 hPa) to the tropopause with a climatological partial column. The profiles are then interpolated to the observational footprints (having a lower spatial resolution), after which the averaging kernel can be directly applied, see Mijling and Van der A (2012].

For this project we have the adapted the existing DECSO algorithm version 5.1 to a new version specifically for the use of TROPOMI data: version 5.2-TROPOMI, which was just in development. This version has also been demonstrated showing emissions at gas pipelines in West Siberia (van der A et al., 2020). More information about the various versions of DECSO can be found in the Appendix.

TROPOMI data

We use the latest official version (version 1.2 and 1.3) of the tropospheric NO2 product of TROPOMI. The Copernicus Sentinel-5P satellite carries the TROPOMI instrument (Veefkind et al, 2012). TROPOMI is a spectrometer combining a high spectral resolution with high spatial resolution (3.5 x 5.5 km^2 at nadir for the NO_2 observations), high signal-to-noise ratios and a daily global coverage. Despite the much smaller footprints, the spectral fits of the individual TROPOMI ground pixels have 30% smaller noise than those from the earlier Ozone Monitoring Instrument (OMI) and the average values agree well to within 5% (van Geffen et al, 2020). Figure 4.1 shows a map of averaged TROPOMI NO2 data over South America.

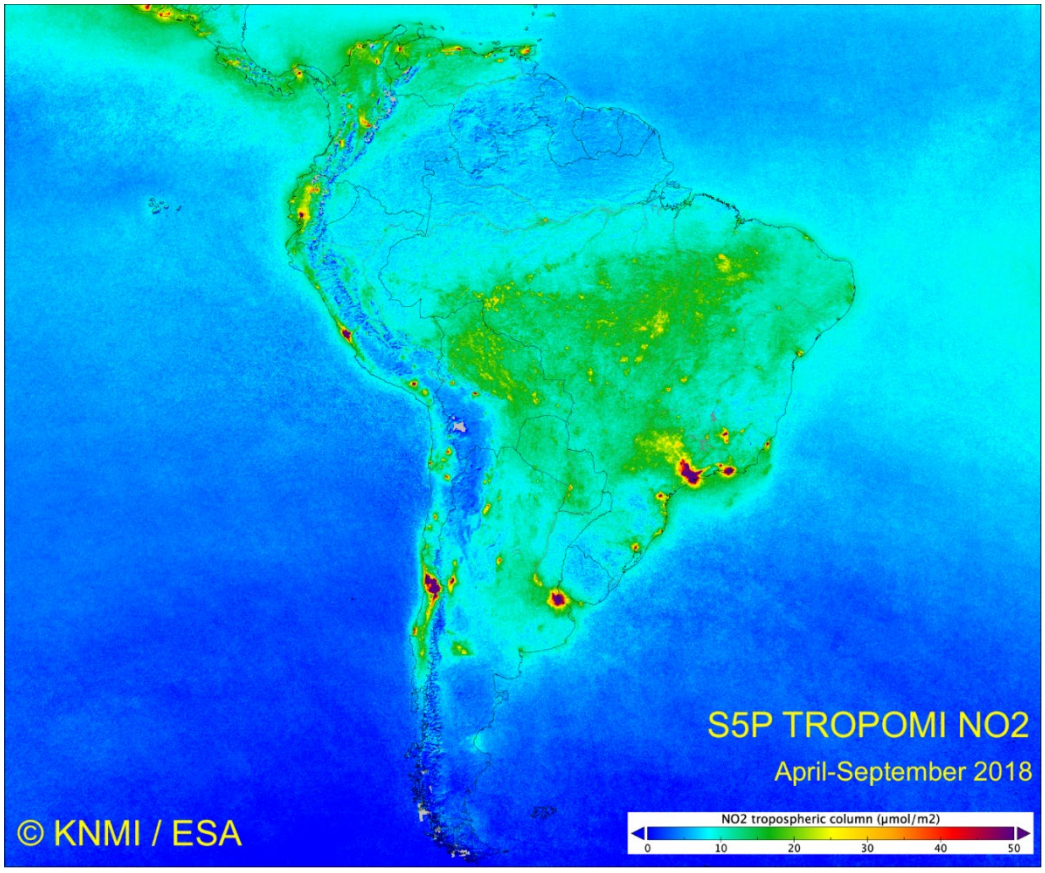

Figure 4.1 *Averaged tropospheric NO2 columns as observed by the S5 TROPOMI instrument in the summer of 2018.*

Implementation of TROPOMI in a new domain

Several technical changes had to be made to successfully implement the DECSO algorithm to the new domain on a 0.125 degree resolution in South America. The most important changes were:

- Timestep of the CHIMERE has been decreased to 7.5 min for better representation of transport on the high resolution grid.
- The lifetime fit of NO_x has been optimized for more precise local lifetimes. (see next section)
- New parametrization of the covariance matrix of the combined model, observation and representation error has been derived.
- The value of the minimum of H-elements (the sensitivity of concentration on emissions changes) has been set to 0.05 to avoid amplification of noise in the inverse calculation.
- The correlation length of emission errors is set to 1 km.
- The regularisation of the inverse calculation has been improved.
- The NO2 climatology for the free troposphere has been corrected.

Because of constraints in calculation speed and memory use we have limited our domain to two parts of South America that are interesting because of their high population density, economic activity and the agricultural activities.

Lifetime fit

Determining the spatial field of the effective lifetime of NO_x is an essential element of the DECSO algorithm. The lifetime is fitted by comparing detailed trajectory analyses with a daily run of the chemical transport model CHIMERE. A constraint is desired in this fit, since the problem is underdetermined and there are multiple solutions possible. The constraint has been designed based on the assumption that the lifetime field is rather smooth. The lifetime is affected by length of day-light, precipitation, temperature and surface type. These are in general slowly varying in spatial directions.

Recently a lot of development has taken place on the TROPOMI version (new resolution, new error descriptions, etc.) and therefore we decided to check if the lifetime fit is still optimal with the current settings of the algorithm. Applying four different constraints, we have determined lifetimes and emissions for July 2018 (starting from February 2018 for spin-up period) for the challenging domain over the Andes: a chosen region from Santiago in the West to Buenos Aires in the East. Figure 4.2 shows the average fitted lifetime for the four cases: (1) default setting, (2) ten times less constraint, (3) hundred times less constraint and (4) no constraint at all.

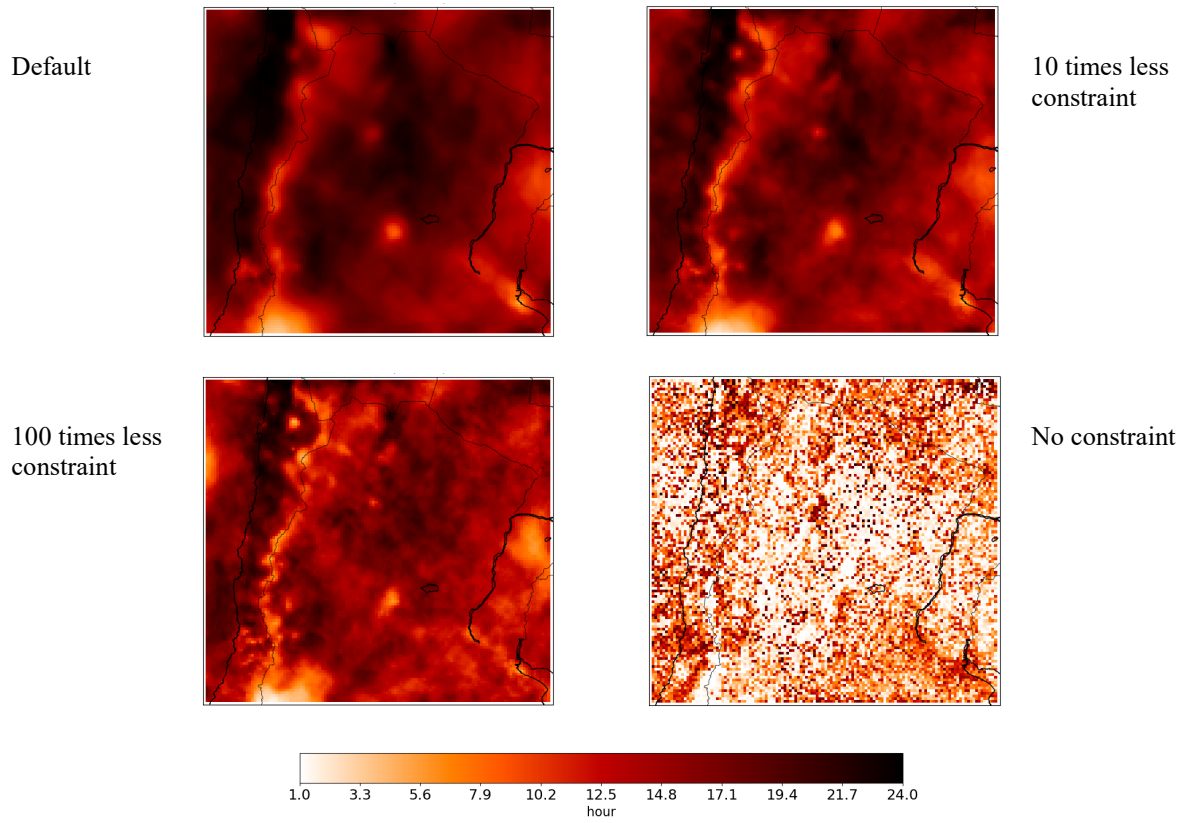

***Figure 4.2**. Resulting effective lifetime using four different constraints. The shown lifetime is an average for the month July 2018.*

The bottom row show the results with the loose constraints, which results in a too variable lifetime field and also with too low lifetimes (less than 1 hour). We know that the lifetime is especially low over cities and reflective surfaces like snow or deserts and it should be longer

over oceans and canopy. This is best reflected in the results on the top row. I prefer the option with 10 times less constraint, because it shows more details and the lifetime in cities is low but still higher than 1-2 hours. The resulting emissions in all cases do not differ so much, which shows that the algorithm is quite stable.

High altitude issue

The CTM used in DECSO is performing the modelling till a pressure level of about 500 hPa. For very high mountain ranges this can lead to too small model layers with unrealistic local model results. This can lead to unrealistic emissions over the Andes. Therefore, all data for grid cells with an average altitude above 3500 m has been removed. Figure 4.3 shows the altitude in the region of the emissions.

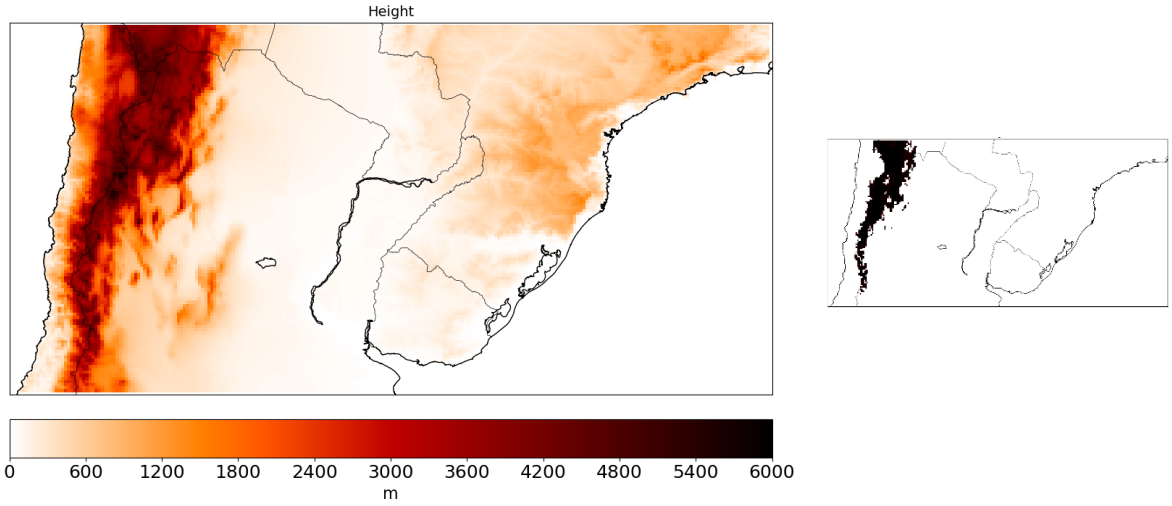

Figure 4.3 *Surface altitude in the region for which the emissions are provided (left).The filtered region is indicated by the black region in the small plot at the right.*

4.2 Results for South America

We have processed the NOx emission data over the middle of South America for the entire period that TROPOMI data is available. The regular observations start in February 2018, but the first months till 1 July 2018 are considered the spin-up period of our data assimilation and the NOx emission data of these months are not released. The daily NOx emission data from 1 July 2018 till 31 March 2020 has been processed and made available as monthly average emissions on the web page:

http://www.globemission.eu/region_samerica/datapage_nox.php

An example of the emission field in our domain is shown in Figure 4.4. Note that this is combined plot of the emissions of two separate regions, hence the grey region at the top of the image, for which no emissions have been derived.

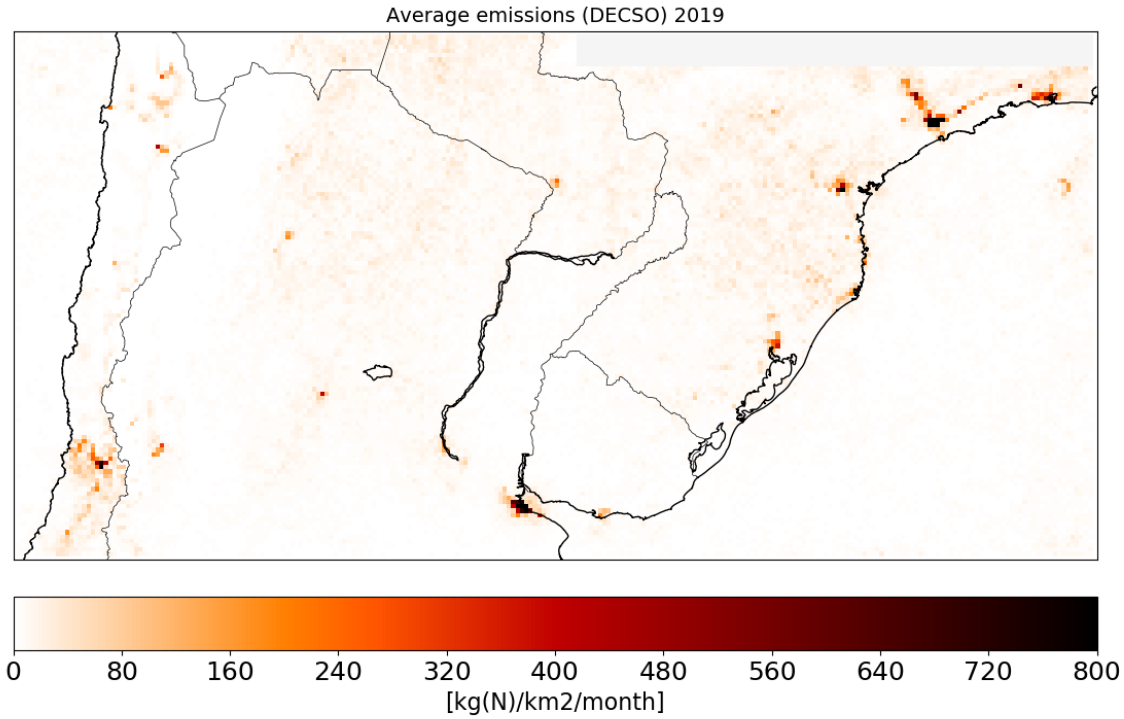

Figure 4.4. *NO_x emission for the year 2019 derived from the TROPOMI satellite using the DECSO algorithm.*

Two examples of times series of typical emissions are given in Figure 4.5. For each time series a region of 3 x 3 pixels (~35 x 35 km) is taken to cover the extent of most cities. The top plot shows the timelines of emissions in the Brazilian cities Sao Paulo, Rio de Janeiro, Porto Alegro, the Argentinean capital Buenos Aires and the Chilean capital Santiago. The cities have higher emissions in wintertime compared to summertime (Southern hemisphere).
In addition, the emissions of the Lula oil field on the Atlantic Ocean south of Rio de Janeiro are shown. The Lula oil field is one of the largest on the Western hemisphere.
The lower plot shows the emissions of an agricultural area in Chaco in North Argentina. The seasonal cycle clearly shows a peak in February and almost no emissions in July when the temperature is low.

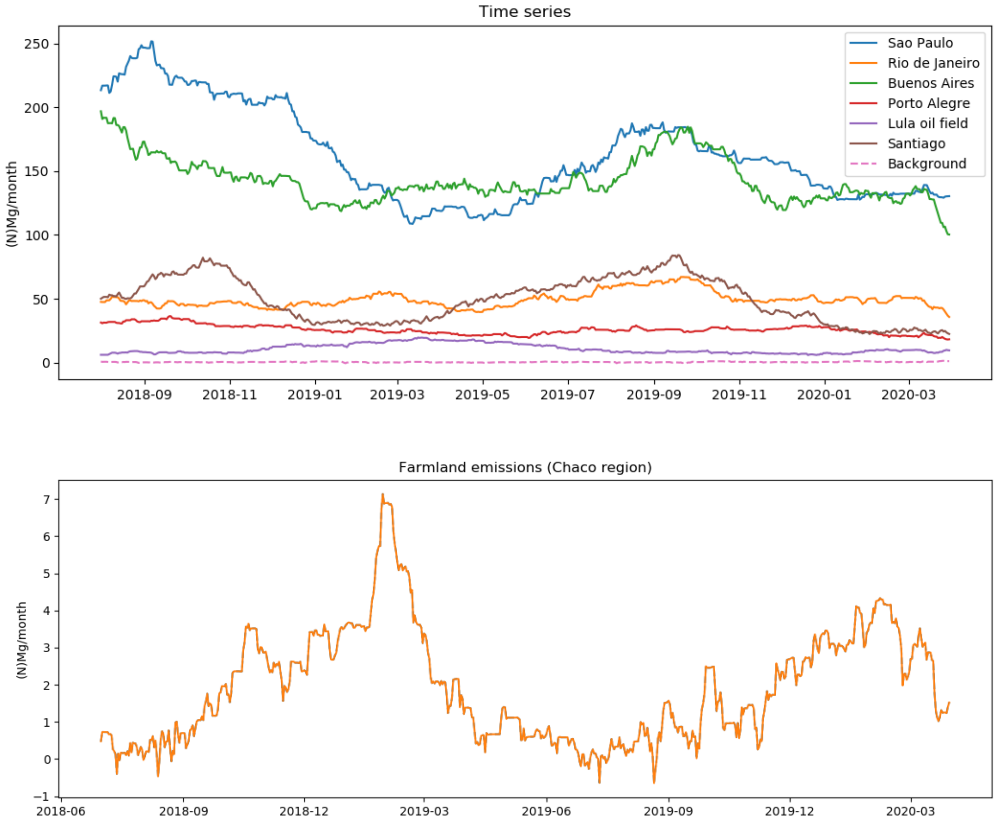

Figure 4.5 *Timeseries of (a) emissions from cities in South America and (b) emissions from an agricultural region in Chaco, Argentina.*

4.3 Validation and Data quality

4.3.1 Summary of TROPOMI NO_2 validation results

The validation activities for TROPOMI versions 1.2 and 1.3 have clearly indicated that the tropospheric NO_2 column product is low compared to independent observations, in particular against MAX-DOAS, PANDORA and aircraft campaign data (e.g. Judd et al., 2020, Tack et al., 2020, Verhoelst et al., 2020). Typically, for the MAX-DOAS instruments a bias of -30% is reported in the routine validation activity (the Mission Performance Centre) for TROPOMI.

Two main observations are of relevance for the emissions:

- Comparisons against MAXDOAS indicate that the bias is multiplicative, increasing linearly with the column amount. The slant column observations and stratospheric column agree well with SAOZ and PANDORA. The linearity indicates that mainly the air-mass factor is involved.
- An analysis of the retrieval attributes the low bias to three main effects: (1) a bias in the cloud pressure retrieval which substantially impacts the low cloud fraction retrievals; (2) a high bias in the albedo, and (3) the coarse resolution of the a-priori profiles (1x1 degree). We estimate that roughly half of the systematic low bias at NO_2 hotspots is related to the a-priori profile shape (point 3). However, this part of the bias does not influence the results presented in our

study. The reason is that we explicitly make use of the TROPOMI averaging kernels, which makes the emission results independent of the retrieval a-priori profile shape.

In conclusion, a typical systematic absolute bias of about 15% will remain, and we expect the emissions to be low by such an amount on average.

4.3.2 Validation of version 5.0 over China

NO_x estimates are done with our in-house developed, state-of the-art DECSO algorithm. Various versions of the DECSO algorithm have been validated in various papers. Validation of the latest version 5.0/5.1 is described in Ding et al. (2018), Ding et al. (2017a), and Ding et al. (2017b). In general, the uncertainty of the monthly averaged NOx emissions is estimated as 20%. Currently, OMI observations are used for NOx emission estimates. We used the QA4ECV retrieval algorithm for the OMI NO_2 data (collection 3). Higher resolution emissions became also available using TROPOMI retrievals, taking advantage of the superior spatial resolution and signal-to-noise ratio of this instrument. These higher resolution emissions of TROPOMI are only processed for smaller domains like the Iberian Peninsula.

4.3.3 Verification of version 5.2 over the Iberian peninsula

Within the CHE project DECSO v5.2 has been compared with TNO industrial 2010 NO_x emissions over the Iberian Peninsula on a 1/8 degree grid. In both data sets dominant NO_x emissions sources can easily be identified: (large) cities, shipping lanes, corridors between large cities consisting of roads and smaller cities and towns along these corridors. There is also a striking difference: DECSO emissions in rural and non-populated areas are much larger than in the TNO database. This is caused by soil emissions, which simply are not present in the TNO industrial 2010 NO_x emission database.

TNO total NO_x emissions for this region are 1.49/1.36 Tg/year for 2010 and 2015, respectively, while total DECSO NO_x emissions for the same region amount to 2.55 Tg/year. If only pixels are considered where TNO NO_x emissions are larger than 0.1 Tg, then DECSO NOx emissions are 1.41/1.37 Tg/year, respectively.

A difference plot of TNO and DECSO NO_x emission (not shown) indicated that there appear to be some pixel-by-pixels shifts in emissions. This can be related to the information going into the bottom-up TNO emission database not being spatially very accurate at the grid scale. For example, emissions often are reported per city region or province. Based on other information, these emissions will then be redistributed to the smaller grid, but this inevitably will introduce spatial uncertainties and inaccuracies, even though the total emissions for the city region or province may be accurate.

To account for this, Figure 4.6 shows a scatterplot of total NO_x emissions per 2°×2° grid, but only considering the 1/8 grid points for which the TNO NO_x emissions were larger than 0.1 Tg/gridpoint. The 2°×2° averaging should – to some extent – account for the spatial uncertainties and inaccuracies introduced by the high resolution redistribution process. Clearly, at this 2°×2° resolution there is an excellent agreement between the TNO and DECSO emissions. The high bias of approximately 20% of TNO compared to DECSO may be related to the years they represent (2010 vs. July 2018 – June 2019).

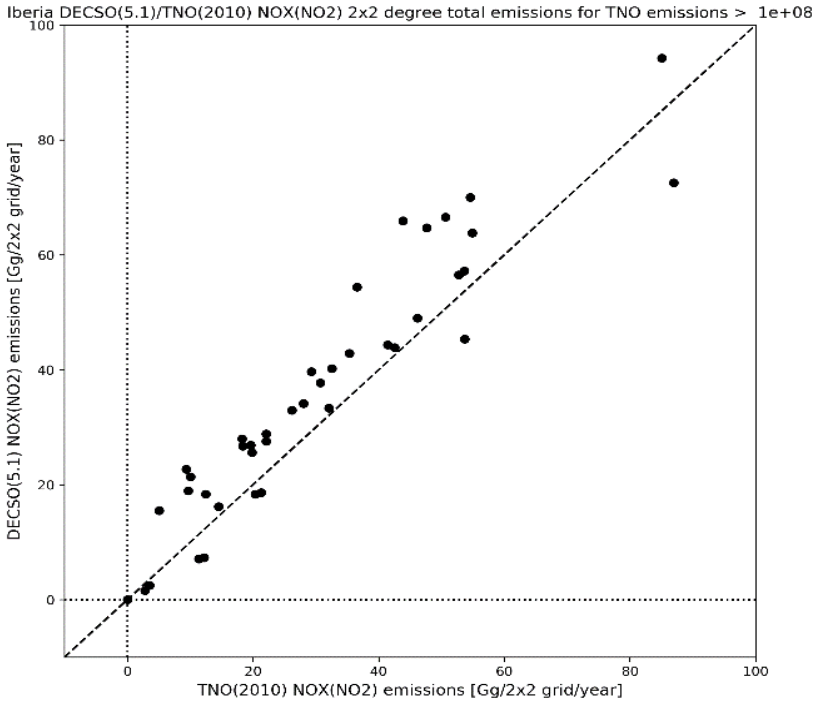

Figure 4.6 *Scatterplot of Iberian TNO (2010) and DECSO (July 2018 – June 2019) total NOx emissions at a 2°x2° grid. To account for the biogenic NOx emission in DECSO that are not part of the TNO database, only 1/8° grid points with TNO emissions larger than 0.1 Gg are included in calculating the 2°x2° grid average.*

4.3.4 Comparison to an Argentinian bottom-up inventory

We have compared the DECOS emission to an Argentinean bottom-up emission inventory recently published in Puliafito et al. (2020). The inventory contains emission for the year 2014 and 2016. We have resampled the 2016 NOx emissions to the same grid as of DECSO for comparison. Figure 4.7 shows the comparison between the annual bottom-up and the annual averaged NOx emissions of DECSO. The inventories disagree on two points:

1. The emissions from traffic in Puliafito et al. are very prominent in the figure, with traffic emissions amounting to 50% of the total emissions. In the DECSO emissions the road-map of Argentina cannot be distinguished. When the traffic emissions are reduced by 75% in Puliafito et al., the emissions are comparable (see Figure 4.8).
2. Agricultural emissions are much higher in the DECSO map as can be seen in the Northern part of Argentina, where many agricultural communities exist.

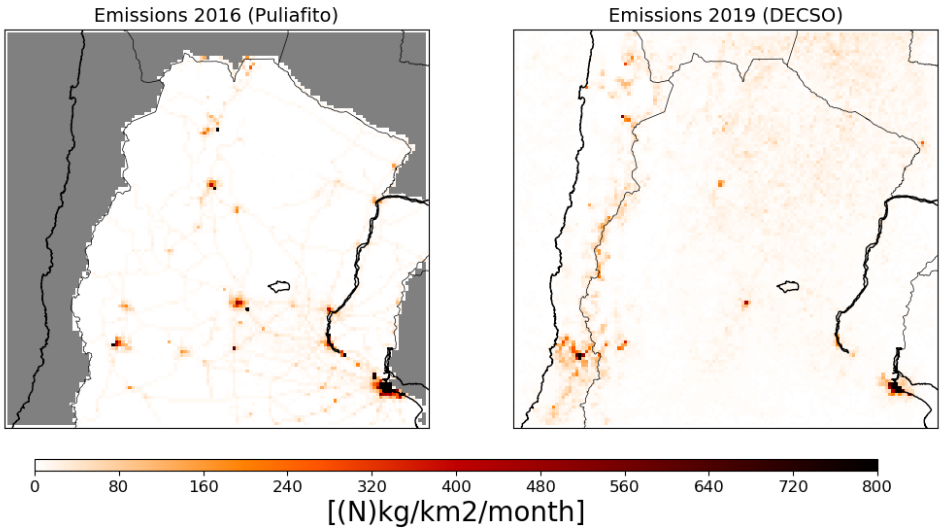

Figure 4.7 *Comparison of the NO_x emissions over Argentina from the bottom-up inventory in 2016 (left plot) and the DECSO emissions in 2019 (right plot).*

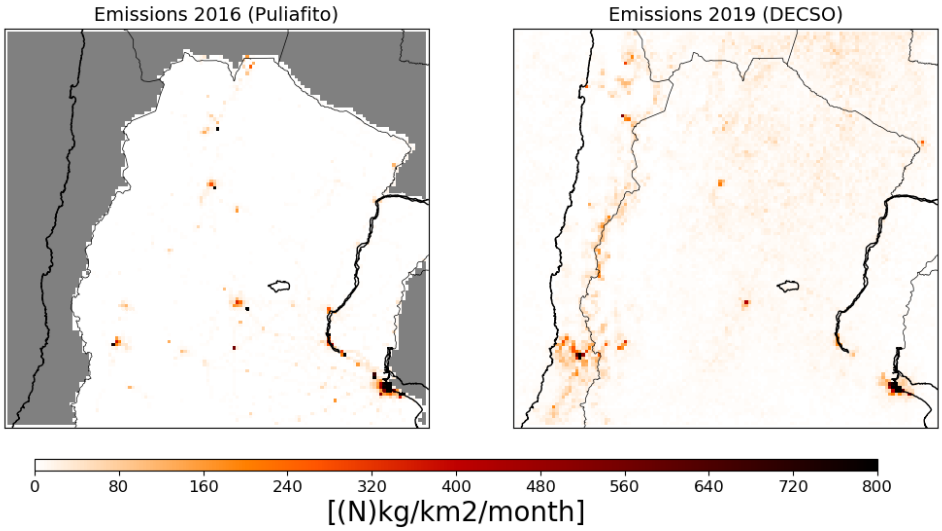

Figure 4.8 *Same as Figure 4.7, but with traffic emissions reduced by 75% in the bottom-up inventory.*

5 Validation of top-down emission estimates (WP5)

5.1 Validation against ground-based measurements

Ground-based FTIR measurements in South America are available from Paramaribo (Surinam) and Porto Velho (Brazil) sites (Vigouroux et al. 2020, 2018). The measurements in Paramaribo cover all years from 2005 to 2018, but they have a very sparse temporal coverage. The measurements in Porto Velho cover all months from July 2016 to July 2017 and from August to November 2019. In Figure 5.1 the FTIR data are compared to the model columns before and after optimization. The a priori model overestimates the bias-corrected OMI observations by about 30% at both sites. With respect to the FTIR columns the a priori model overestimates the HCHO column by 26% in Porto Velho and by about 20% in Paramaribo. The bias is strongly reduced after optimization, especially at Porto Velho. In comparison with the FTIR data the a posteriori model columns are in much closer agreement with the observation as seen by the improved correlation and the reduced bias. Note that the very low values and higher relative error in the satellite columns at Paramaribo compared to Porto Velho explain the higher a posteriori bias at this site. Finally, note that the FTIR measurements were used for correcting the biases in the satellite HCHO columns, as explained in Section 3.2. The good a posteriori match of the model with FTIR data confirms the robustness of the bias correction.

Note that we presented only validation against OMI-based emission estimates, because of the lack of validation data in South America in 2018.

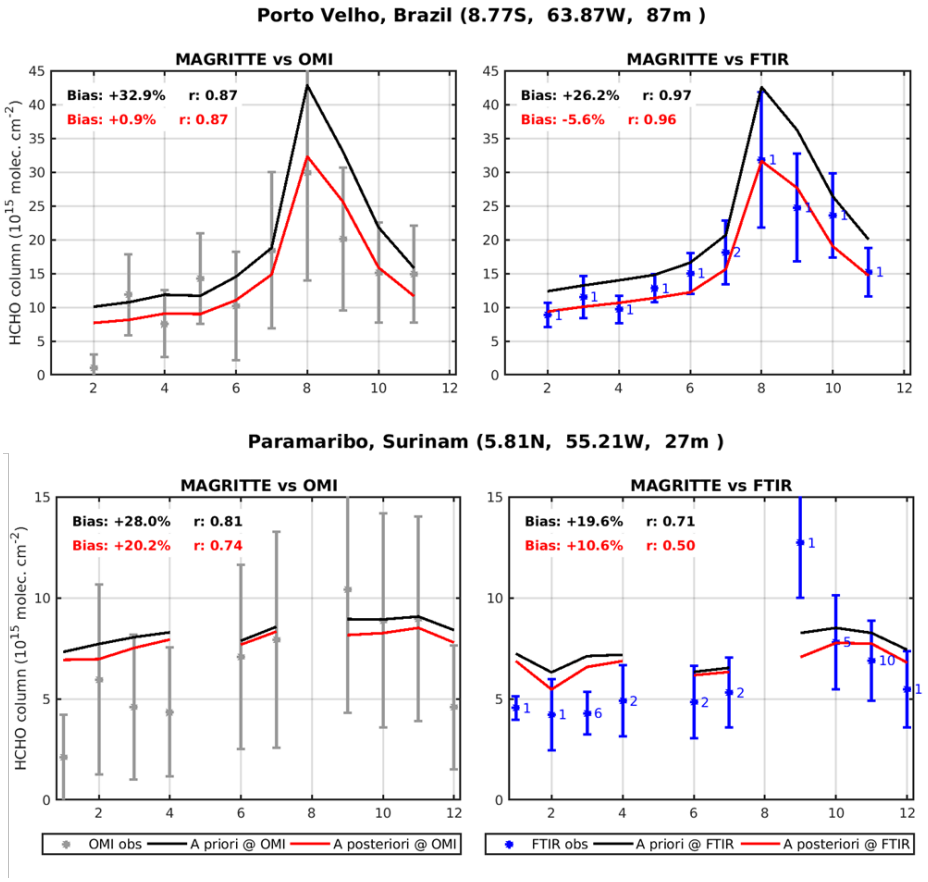

***Figure 5.1**: A priori (black) and a posteriori (red) HCHO columns compared to observed columns from OMI (grey) and FTIR (blue). The numbers in blue denote the number of available monthly measurements for a given month based on all available FTIR data between 2005 and 2017.*

5.2 Validation against aircraft data

The GABRIEL airborne campaign took place in October 2005 in the pristine forests of Surinam, Guyana and French Guiana (6–3°N, 50–59°W). The campaign is described in detail in Eerdekens et al. (2009) and Lelieveld et al. (2008). To perform a meaningful comparison with the model, we extracted the model output at time of flight and location of the measurements calculated through forward simulations using either a priori or top-down emissions. As shown in Table 5, the top-down constraints bring the model to a satisfactory agreement with the aircraft measurements. The a priori strong model overestimation for isoprene (factor of 2) and HCHO (46%) concentrations in the boundary layer turns into a good agreement after the inversion, whereas the optimized NO concentrations are found to lie closer to the observed values. Note that the OH measurement relied on the FAGE technique, shown to be affected by internally generated OH (Mao et al., 2012). This artefact might partly explain the large model underestimation.

Compounds	Obs (std)	A priori	Optimized
Isoprene (ppb)	2 (0.76)	4.41	1.58
HCHO (ppb)	1.15 (0.86)	1.68	1.21
NO (ppt)	20 (20)	14	18
OH (10^6 molec. cm^{-3})	5.9 (1.9)	2.19	3.15
O_3 (ppb)	18.5 (4.6)	21.9	22.8

Table 5: Concentrations measured during the GABRIEL campaign compared to the modelled a priori and a posteriori.

5.3 Validation against flux measurements

In Figure 5.2 the a priori and top-down isoprene emission estimates are directly compared to field campaign measurements performed at 6 locations in Amazonia. The observed fluxes have been compiled from 14 literature studies (Alves et al., 2016, 2018; Andreae and Merlet, 2001; Ciccioli et al., 2003; Davis et al., 1994; Greenberg et al., 2004; Helmig et al., 1998; Karl et al., 2007; Kuhn et al., 2007; Rinne et al., 2002; Rizzo et al., 2010; Sarkar et al., 2020; Simon et al., 2005; Zimmerman et al., 1988). The comparison accounts for the diurnal variations in the fluxes through correction factors used to scale the measured fluxes to daily averages. Direct comparisons between modeled fluxes and field measurements should, however, be considered with caution mainly due to the coarse resolution of the modeled emissions, but also to the fact that flux measurements were often performed outside the study period (2005–2017). The observed isoprene fluxes exhibit strong local differences within the forest, significant differences from one day to another, whereas they may exhibit differences due to different measurement techniques. Overall, the emission reduction derived by the satellite observations lies within the variability of the field measurements, while the discrepancies between the observed fluxes are often larger than the differences between the a priori and top-down fluxes. The field studies generally agree on higher fluxes during the dry and the dry-to-wet transition season between July and December), that are also suggested by the model. Finally, the much

lower fluxes (by ca. a factor of 3) observed by Alves et al. (2016) compared to the top–down estimates are most likely related to a local effect of leaf flushing at the measurement location.

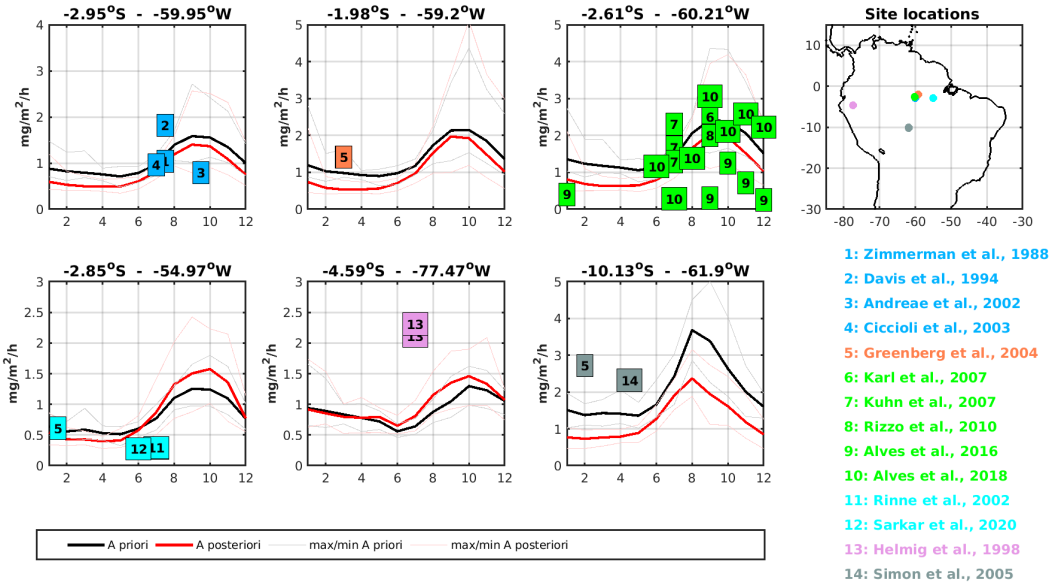

***Figure 5.2**: A priori (black) and satellite-based (red) isoprene fluxes compared with flux measurements (colored numbered squares) obtained at the measurement sites shown on the map. The model fluxes are averaged over 2005-2017 for the model grid cells of the measurement locations.*

5.4 Validation against independent inventories

The a priori and the OMI-based isoprene emission estimates have been compared to GUESS-ES (Arneth et al., 2007), MEGAN-MACC (Sindelarova et al., 2014) and the most recent Copernicus inventory, CAMS-BIO (Granier et al., 2019). Figure 5.3 illustrates the spatial distribution of these three independent emission inventories for 2009. The OMI-based emissions are by about 20% lower than GUESS-ES and MEGAN-MACC inventories, but lie close to CAMS-BIO estimates, which are based on the MEGAN model. The spatial patterns of CAMS-BIO agree well and the OMI-based emissions, but the top-down emissions suggest lower fluxes over western and south Amazonian rainforests. The seasonal variation of CAMS-BIO and OMI-based emissions are in good agreement, although the OMI-based emissions are slightly lower during the wet season. In comparison to the inferred OMI-based estimates, the GUESS-ES model shows uniform spatial patterns and a much smaller amplitude of the seasonal cycle compared to the other inventories.

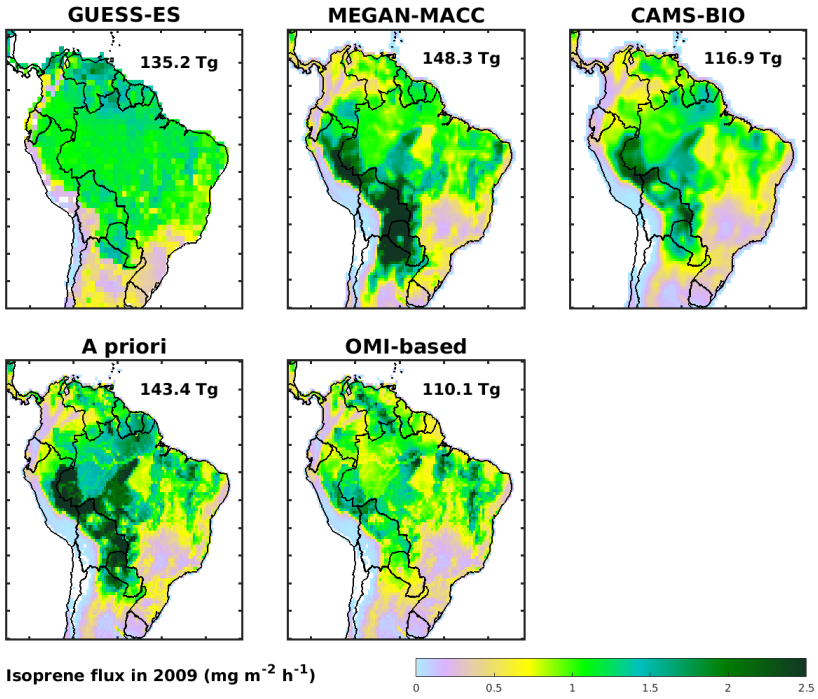

***Figure 5.3**: Comparison of a priori and OMI-based isoprene emission estimates with three independent bottom-up emission inventories for 2009. The annual emission for the domain is given inset each panel.*

In Figure 5.4 the a priori (GFED4s) and the OMI-based fire emission estimates are compared to the GFAS fire emission inventory obtained by assimilation of MODIS fire radiative power (Kaiser et al., 2012). The satellite data indicate a strong reduction of the emission (about 30%) in years with intense fire activity (2007 and 2010), whereas the top-down emissions stay close to the a priori for years with low fire activity (2009 and 2011). In years with intense fires, the emission reductions are important in the southern part of the Amazon forest, whereas slight emission increases are suggested by the inversion over Colombia, western Venezuela and the Minas Gerais province in Brazil. The comparison between GFEDv4s and GFAS (right panel) indicates similar spatial patterns, with lower GFAS emissions (-15 to -25%) for years with intense fires compared to GFED4s, and lower emissions in the southern part of Amazonia. The differences in spatial patterns between GFED4s and GFAS are however bigger than the differences between the GFED4s and the OMI-based fluxes. Note also, that compared to GFEDv4, GFAS suggests higher fire emissions in years with low fire emissions, which is not the case for with the OMI-based estimates. This comparison indicates the often large differences between fire emission estimates derived by satellite proxy data, like fire radiative power and burnt area used in GFAS and GFED4s, respectively.

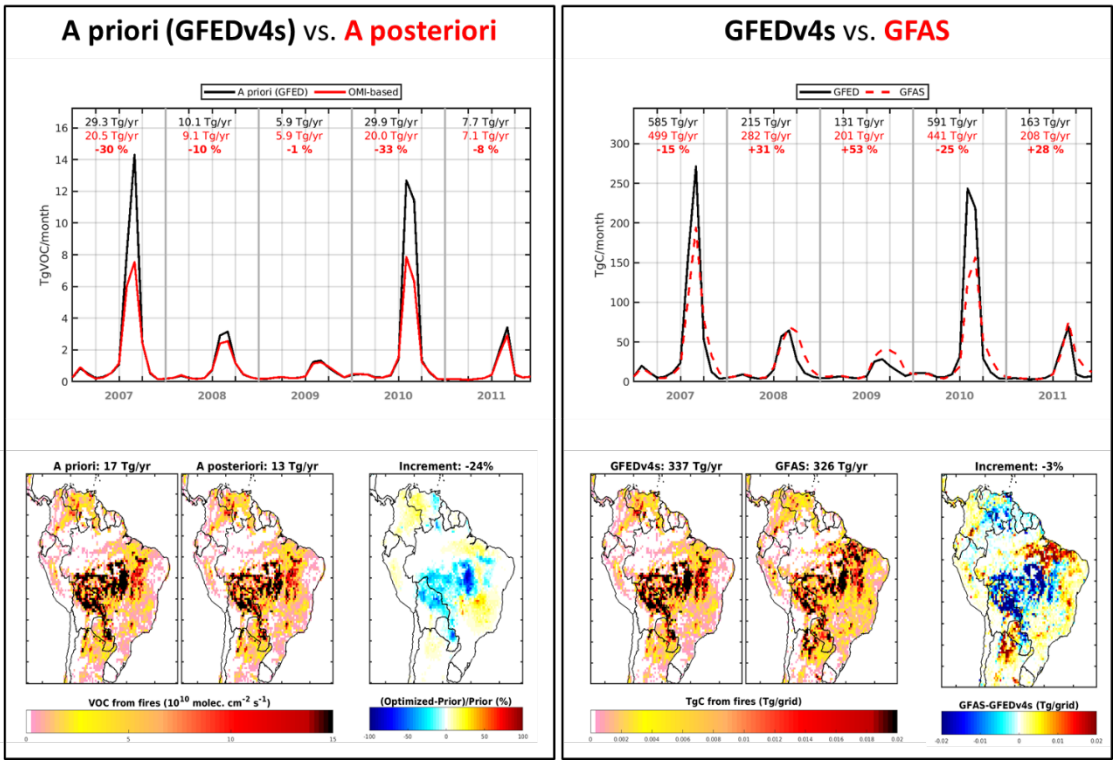

***Figure 5.4**: Comparison of a posteriori fire emission estimates to the GFAS biomass burning inventory. In the upper panel monthly biomass burning fluxes are shown in TgVOC (left) and Tg C (right). In the lower panels, the spatial distributions and difference maps are provided.*

6 Dissemination (WP6)

Websites, open access datasets and user guides

The SOLFEO project is described on the following ESA web-page
https://eo4society.esa.int/projects/solfeo-spaceborne-observations-over-latin-america-for-emission-optimization-applications/

The top-down emission estimates derived within SOLFEO and the related user guides are disseminated via the GlobEmission data portal (www.globemission.eu).

Ammonia (NH_3) emissions:

http://www.globemission.eu/region_samerica/datapage_nox.php
http://www.globemission.eu/region_samerica/datapage_nh3.php
http://www.globemission.eu/docs/SOLFEO_NH3_PUG.pdf
http://www.globemission.eu/docs/SOLFEO_NOx_PUG.pdf

Isoprene:

https://emissions.aeronomie.be/index.php/tropomi-based/isoprene-sa
https://emissions.aeronomie.be/index.php/omi-based/isoprene-sa
https://emissions.aeronomie.be/ProjectDir/Readme_TROPOMI_ISOP_SA.pdf
https://emissions.aeronomie.be/ProjectDir/Readme_OMI_ISOP_SA.pdf

Fire emissions:

https://emissions.aeronomie.be/index.php/tropomi-based/fire-sa
https://emissions.aeronomie.be/index.php/omi-based/fire-sa
https://emissions.aeronomie.be/ProjectDir/Readme_TROPOMI_FIRES_SA.pdf
https://emissions.aeronomie.be/ProjectDir/Readme_OMI_FIRES_SA.pdf

NOx emissions:

http://www.globemission.eu/region_samerica/datapage_nox.php
http://www.globemission.eu/docs/SOLFEO_NOx_PUG.pdf

Peer-reviewed publications

Worden, H. M., Bloom, A. A., Worden, J. R., Jiang, Z., Marais, E., **Stavrakou, T.,** Gaubert, B., and Lacey, F.: New Constraints on Biogenic Emissions using Satellite-Based Estimates of Carbon Monoxide Fluxes, *Atmos. Chem. Phys.*, 19, 13569–13579, https://www.atmos-chem-phys.net/19/13569/2019, 2019. (Including acknowledgement to the GlobEmission project)

Yañez-Serrano, A. M., Bourtsoukidis E., Alves, E., **Bauwens, M., Stavrakou, T.**, Llusia, J. et al.: Amazonian BVOC emissions under global change: a review of current research and future directions, *Glob. Chang. Biol.,* https://doi.org/10.1111/gcb.15185, 2020. (Including acknowledgement to the SOLFEO project)

Oral Presentations

"How well can we constrain non-methane volatile organic compound emissions over South America using OMI and TROPOMI formaldehyde data?" (invited), **T. Stavrakou, J.-F. Müller, M. Bauwens**, B. Franco, L. Clarisse, P. Coheur, C. Clerbaux, AGU Fall Meeting, San Francisco, 9-13 December 2019.

"Distribution and trends of biogenic emissions over South American ecosystems deduced by multiyear inversion of satellite formaldehyde data", **T. Stavrakou, J.-F. Müller, M. Bauwens**, I. De Smedt, M. Van Roozendael, 19th GEIA Science Conference 19th GEIA Virtual Science Conference, 23 June 2020.

"*Improving the temperature dependence of modeled isoprene emissions in MEGAN with remote sensing constraints*", C. DiMaria, D. Jones, A. Bloom, H. Worden, K. Miyazaki, K. Bowman, **T. Stavrakou**, AGU Virtual Fall Meeting, 7-11 December 2020.

Poster Presentations

"Deriving NH3 and NOx emissions in South America from satellite observations", **Ronald van der A, Jieying Ding,** 19th GEIA Virtual Science Conference, 23 June 2020

*"Thirteen years of top-down VOC emission estimates over South America inferred by inversion of OMI formaldehyde observations"***, M. Bauwens, T. Stavrakou, J.-F. Müller**, I. De Smedt, C. Vigouroux, M. Van Roozendael, EGU 2019, Vienna, 7-12 April 2019.

Press release

First TROPOMI-based emission estimates over South America, 19 February 2020:

https://eo4society.esa.int/2020/02/19/first-tropomi-based-emission-estimates-over-south-america

https://twitter.com/KNMI/status/1230426171092979712

User contacts

Contacts with our users have become complicated, first by the postponement of the GEIA conference and related meetings due to the civil unrest in Santiago and later by the COVID19 crisis, in which travel and physical meetings with users were no longer possible.

Although the user contact have been limited we still had a meeting with Eduardo Landulfo of IPEN in Sao Paulo, would like to cooperate on studies to (1) emissions in São Paulo as a Megacity and from agricultural/industry (oil exploration) in the São Paulo region, and (2) emissions in Brazil and South America due to biomass burning issue. There is also interest in our top-down estimates from the AMIGO community and in particular Dylan Jones (Canada) and Helen Worden (PI of MOPITT).

The collaborations on these topics will be continued in the future.

7 References

Alves, E. G., Jardine, K., Tota, J., Jardine, A., Yãnez-Serrano, A. M., Karl, T., Tavares, J., Nelson, B., Gu, D., Stavrakou, T. et al.: Martin, S., Artaxo, P., Manzi, A., and Guenther, A.: Seasonality of isoprenoid emissions from a primary rainforest in central Amazonia, Atmos. Chem. Phys., 16, 3903–3925, https://doi.org/10.5194/acp-16-3903-2016, 2016.

Alves, E. G., Tóta, J., Turnipseed, A., Guenther, A. B., Vega Bustillos, J. O. W., Santana, R. A., Cirino, G. G., Tavares, J. V., Lopes, A. P., Nelson, B. W., Souza, R. A. de, Gu, D., Stavrakou, T., Adams, D. K., Wu, J., Saleska, S. and Manzi, A. O.: Leaf phenology as one important driver of seasonal changes in isoprene emissions in central Amazonia, Biogeosciences, 15(13), 4019–4032, doi:10.5194/bg-15-4019-2018, 2018.

Andreae, M. O. and Merlet, P.: Emission of trace gases and aerosols from biomass burning, Glob. Biogeochem. Cy., 15, 955–966, 2001.

Arneth, A., Niinemets, U., Wolf, A., Smith, B., Pressley, S., Back, J., Hari, P., Karl, T., Noe, S., Prentice, I. C. et al.: Process-based estimates of terrestrial ecosystem isoprene emissions: Incorporating the effects of a direct CO-isoprene interaction, Atmos. Chem. Phys., 7(1), 31–53, 2007.

Barkley, M. P., Smedt, I. D., Van Roozendael, M., Kurosu, T. P., Chance, K., Arneth, A., Hagberg, D., Guenther, A., Paulot, F., Marais, E. et al.: Top-down isoprene emissions over tropical South America inferred from SCIAMACHY and OMI formaldehyde columns, J. Geophys. Res., 118(12), 6849–6868, 2013.

Bauwens, M., Stavrakou, T., Müller, J.-F., Smedt, I. D., Roozendael, M. V., Werf, G. R., Wiedinmyer, C., Kaiser, J. W., Sindelarova, K. and Guenther, A.: Nine years of global hydrocarbon emissions based on source inversion of OMI formaldehyde observations, Atmos. Chem. Phys., 16, 10133–10158, 2016.

Ciccioli, P., Brancaleoni, E., Frattoni, M., Marta, S., Brachetti, A., Vitullo, M., Tirone, G. and Valentini, R.: Relaxed eddy accumulation, a new technique for measuring emission and deposition fluxes of volatile organic compounds by capillary gas chromatography and mass spectrometry, J. Chromatogr. A, 985(1-2), 283–296, 2003.

Dammers, E., Palm, M., Van Damme, M., Vigouroux, C., Smale, D., Conway, S., Toon, G. C., Jones, N., Nussbaumer, E., Warneke, T., Petri, C., Clarisse, L., Clerbaux, C., Hermans, C., Lutsch, E., Strong, K., Hannigan, J. W., Nakajima, H., Morino, I., Herrera, B., Stremme, W., Grutter, M., Schaap, M., Wichink Kruit, R. J., Notholt, J., Coheur, P.-F., and Erisman, J. W.: An evaluation of IASI-NH3 with ground-based Fourier transform infrared spectroscopy measurements, Atmos. Chem. Phys., 16, 10351–10368, https://doi.org/10.5194/acp-16-10351-2016, 2016.

Dammers, E., McLinden, C. A., Griffin, D., Shephard, M. W., Van Der Graaf, S., Lutsch, E., et al.. (2019). NH_3 emissions from large point sources derived from CrIS and IASI satellite observations. Atmos. Chem. Phys., 19(19), 12261-12293. doi:10.5194/acp-19-12261-2019

Davis, K., Lenschow, D. and Zimmerman, P.: Biogenic nonmethane hydrocarbon emissions estimated from tethered balloon observations, Journal of Geophysical Research: Atmospheres, 99(D12), 25587–25598, 1994.

Ding, J., Miyazaki, K., van der A, R.J., Mijling, B., Kurokawa, J., Cho, S., Janssens-Maenhout, G., Zhang, Q., Liu, F., and Levelt, P.F., Intercomparison of NOx emission inventories over East Asia, Atm. Chem. Phys., 2017a, 17, 10125-10141, doi:doi.org/10.5194/acp-17-10125-2017.

Ding, J., R.J. van der A, B. Mijling and P.F. Levelt, Space-based NOx emission estimates over remote regions improved in DECSO, Atmospheric Measurement Techniques, 2017b, 10, 925-938, doi:10.5194/amt-10-925-2017.

Ding, J., van der A, R. J., Mijling, B., Jalkanen, J.-P., Johansson, L. and Levelt, P. F., Maritime NOx emissions over Chinese seas derived from satellite observations. Geophysical Research Letters, 45. https://doi.org/10.1002/2017GL076788, 2018.

Eerdekens, G., Ganzeveld, L., Arellano, J. Vilà-Guerau de, Klüpfel, T., Sinha, V., Yassaa, N., Williams, J., Harder, H., Kubistin, D., Martinez, M. and Lelieveld, J.: Flux estimates of isoprene, methanol and acetone from airborne PTR-MS measurements over the tropical rainforest during the GABRIEL 2005 campaign, Atmos. Chem. Phys., 9(13), 4207–4227, doi:10.5194/acp-9-4207-2009, 2009.

Granier, C., Darras, S., Gon H., D. van der, Doubalova, J., Elguindi, N., Galle, B., Gauss, M., Guevara, M., Jalkanen, J.-P., Kuenen, J., Liousse, C., Quack, B., Simpson, D. and K., S.: The Copernicus Atmosphere Monitoring Service global and regional emissions, Report April 2019, doi:doi:10.24380/d0bn-kx16, 2019.

Greenberg, J. P., Guenther, A. B., Pétron, G., Wiedinmyer, C., Vega, O., Gatti, L. V., Tota, J. and Fisch, G.: Biogenic VOC emissions from forested Amazonian landscapes, Glob. Chang. Biol., 10(5), 651–662, 2004.

Hansen, J., Sato, M. and Ruedy, R.: Global temperature update through 2012, National Aeronautics and Space Administration, Goddard Institute for Space Studies. http://www. nasa. gov/pdf/719139main_2012_GISTEMP_summary. pdf, 2013.

Hansen, M. C., Wang, L., Song, X.-P., Tyukavina, A., Turubanova, S., Potapov, P. V. and Stehman, S. V.: The fate of tropical forest fragments, Science Advances, 6(11), eaax8574, 2020.

Helmig, D., Balsley, B., Davis, K., Kuck, L. R., Jensen, M., Bognar, J., Smith Jr, T., Arrieta, R. V., Rodrıguez, R. and Birks, J. W.: Vertical profiling and determination of landscape fluxes of biogenic nonmethane hydrocarbons within the planetary boundary layer in the Peruvian Amazon, J. Geophys. Res., 103(D19), 25519–25532, 1998.

Judd, L. M., Al-Saadi, J. A., Szykman, J. J., Valin, L. C., Janz, S. J., Kowalewski, M. G., et al. (2020). Evaluating Sentinel-5P TROPOMI tropospheric NO2 column densities with airborne and Pandora spectrometers near New York City and Long Island Sound. Atmos. Meas. Tech. Discuss., 2020, 1-52. doi:10.5194/amt-2020-151

Kaiser, J., Heil, A., Andreae, M., Benedetti, A., Chubarova, N., Jones, L., Morcrette, J.-J., Razinger, M., Schultz, M., Suttie, M. aet al.: Biomass burning emissions estimated with a global fire assimilation system based on observed fire radiative power, Biogeosciences, 9(1), 527–554, https://doi.org/10.5194/bg-9-527-2012, 2012.

Karl, T., Guenther, A., Yokelson, R. J., Greenberg, J., Potosnak, M., Blake, D. R. and Artaxo, P.: The tropical forest and fire emissions experiment: Emission, chemistry, and transport of biogenic volatile organic compounds in the lower atmosphere over Amazonia, J. Geophys. Res., 112(D18), 2007.

Kuhn, U., Andreae, M. O., Ammann, C., Araújo, A., Brancaleoni, E., Ciccioli, P., Dindorf, T., Frattoni, M., Gatti, L. V., Ganzeveld, L. et al.: Isoprene and monoterpene fluxes from Central Amazonian rainforest inferred from tower-based and airborne measurements, and implications on the atmospheric chemistry and the local carbon budget, Atmos. Chem. Phys., 7, 2855-2879, 2007.

Lelieveld, J., Butler, T., Crowley, J., Dillon, T., Fischer, H., Ganzeveld, L., Harder, H., Lawrence, M., Martinez, M., Taraborrelli, D. et al.: Atmospheric oxidation capacity sustained by a tropical forest, Nature, 452(7188), 737, 2008.

Mao, J., Ren, X., Zhang, L., Van Duin, D. M., Cohen, R. C. et al.: Insights into hydroxyl measurements and atmospheric oxidation in a California forest, Atmos. Chem. Phys., 12, 8009–8020, https://doi.org/10.5194/acp-12-8009-2012, 2012.

Mijling, B., and van der A, R. J, Using daily satellite observations to estimate emissions of short-lived air pollutants on a mesoscopic scale. *Journal of Geophysical Research: Atmospheres*, 117(D17). doi:10.1029/2012JD017817, 2012

Müller, J.-F. and Stavrakou, T.: Inversion of CO and NOx emissions using the adjoint of the IMAGES model, Atmos. Chem. Phys., 5(5), 1157–1186, doi:10.5194/acp-5-1157-2005, 2005.

Müller, J.-F., Stavrakou, T. and Peeters, J.: Chemistry and deposition in the Model of Atmospheric composition at Global and Regional scales using Inversion Techniques for Trace gas Emissions (MAGRITTE v1.1) – Part 1: Chemical mechanism, Geosci. Mod. Dev., 12(6), 2307–2356, doi:10.5194/gmd-12-2307-2019, 2019.

Peeters, J., Müller, J.-F., Stavrakou, T. and Nguyen, V. S.: Hydroxyl radical recycling in isoprene oxidation driven by hydrogen bonding and hydrogen tunneling: The upgraded LIM1 mechanism, J. Phys. Chem., 118(38), 8625–8643, 2014.

Puliafito, S.E., T. Bolaño-Ortiz, L. Berná, R. P. Flores, High resolution inventory of atmospheric emissions from livestock production, agriculture, and biomass burning sectors of Argentina, Atm. Environment, 223, 117248, doi:10.1016/j.atmosenv.2019.117248, 2020.

Rinne, H., Guenther, A., Greenberg, J. and Harley, P.: Isoprene and monoterpene fluxes measured above Amazonian rainforest and their dependence on light and temperature, Atmos. Environ., 36(14), 2421–2426, 2002.

Rizzo, L., Artaxo, P., Karl, T., Guenther, A. and Greenberg, J.: Aerosol properties, in-canopy gradients, turbulent fluxes and VOC concentrations at a pristine forest site in Amazonia, Atmos. Environ., 44(4), 503–511, 2010.

Sarkar, C., Guenther, A. B., Park, J.-H., Seco, R., Alves, E., Batalha, S., Santana, R., Kim, S., Smith, J., Tóta, J. et al.: PTR-TOF-MS eddy covariance measurements of isoprene and monoterpene fluxes from an eastern Amazonian rainforest, Atmos. Chem. Phys., 20(12), 7179–7191, 2020.

Simon, E., Meixner, F. X., Rummel, U., Ganzeveld, L., Ammann, C. and Kesselmeier, J.: Coupled carbon-water exchange of the Amazon rain forest, II. Comparison of predicted and observed seasonal exchange of energy, CO_2, isoprene and ozone at a remote site in Rondônia, Biogeosciences, 2, 255-275, 2005.

Sindelarova, K., Granier, C., Bouarar, I., Guenther, A., Tilmes, S., Stavrakou, T., Müller, J.-F., Kuhn, U., Stefani, P. and Knorr, W.: Global data set of biogenic VOC emissions calculated by the MEGAN model over the last 30 years, Atmos. Chem. Phys., 14(17), 9317–9341, doi:10.5194/acp-14-9317-2014, 2014.

De Smedt, I., Theys, N., Yu, H., Danckaert, T., Lerot, C., Compernolle, S., Van Roozendael, M., Richter, A., Hilboll, A., Peters, E., Pedergnana, M., Loyola, D., Beirle, S., Wagner, T., Eskes, H., Geffen, J. van, Boersma, K. F. and Veefkind, P.: Algorithm theoretical baseline for formaldehyde retrievals from S5P TROPOMI and from the QA4ECV project, Atmos. Meas. Tech., 11(4), 2395–2426, doi:10.5194/amt-11-2395-2018, 2018.

Stavrakou, T., Peeters, J. and Müller, J.-F.: Improved global modelling of HO_x recycling in isoprene oxidation: evaluation against the GABRIEL and INTEX-A aircraft campaign measurements, Atmos. Chem. Phys., 10(20), 9863–9878, doi:10.5194/acp-10-9863-2010, 2010.

Stavrakou, T., Guenther, A., Razavi, A., Clarisse, L., Clerbaux, C., Coheur, P.-F., Hurtmans, D., Karagulian, F., De Mazière, M., Vigouroux, C., Amelynck, C., Schoon, N., Laffineur, Q., Heinesch, B., Aubinet, M., Rinsland, C., and Müller, J.-F.: First space-based derivation of the global atmospheric methanol emission fluxes, Atmos. Chem. Phys., 11, 4873–4898, https://doi.org/10.5194/acp-11-4873-2011, 2011.

Stavrakou, T., Müller, J.-F., Bauwens, M., De Smedt, I., Van Roozendael, M., Guenther, A., Wild, M. and Xia, X.: Isoprene emissions over Asia 1979–2012: impact of climate and land-use changes, Atmos. Chem. Phys., 14(9), 4587–4605, doi:10.5194/acp-14-4587-2014, 2014.

Stavrakou, T., Müller, J.-F., Bauwens, M., De Smedt, I., Lerot, C., Van Roozendael, M., Coheur, P.-F., Clerbaux, C., Boersma, K., Song, Y.: Substantial underestimation of post-harvest burning emissions in the North China Plain revealed by multi-species space observations, Sci. Rep., 6, 32307, 2016.

Tack, F., Merlaud, A., Iordache, M. D., Pinardi, G., Dimitropoulou, E., Eskes, H., et al. (2020). Assessment of the TROPOMI tropospheric NO2 product based on airborne APEX observations. Atmos. Meas. Tech. Discuss., 2020, 1-55. doi:10.5194/amt-2020-148

Van Damme, M., Whitburn, S., Clarisse, L., Clerbaux, C., Hurtmans, D., and Coheur, P.-F.: Version 2 of the IASI NH_3 neural network retrieval algorithm: near-real-time and reanalysed datasets, Atmos. Meas. Tech., 10, 4905–4914, https://doi.org/10.5194/amt-10-4905-2017, 2017.

Van Damme, M., Clarisse, L., Whitburn, S., Hadji-Lazaro, J., Hurtmans, D., Clerbaux, C., & Coheur, P.-F. (2018). Industrial and agricultural ammonia point sources exposed. Nature, 564(7734), 99-103. doi:10.1038/s41586-018-0747-1

van der A, Ronald, Jenny Stavrakou, Maite Bauwens, Nele Veldeman, Bino Maiheu, Lyana Curier, Mikhail Sofiev, Gerrit de Leeuw, Edith Rodriguez; Julius Vira, Bas Mijling, Claus Zehner , Algorithm Theoretical Baseline Document, GE-ATBD, Version 3.4, 2016

van der A, R.J., de Laat, A.T.J., Ding, J., Eskes, H.J., Connecting the dots: NOx emissions along a West Siberian natural gas pipeline, npj Clim Atmos Sci 3, 16, https://doi.org/10.1038/s41612-020-0119-z, 2020.

van Geffen, J. H. G. M., Eskes, H. J., Boersma, K. F., Maasakkers, J. D., and Veefkind, J. P. (2019). TROPOMI ATBD of the total and tropospheric NO_2 data products, Report S5P-KNMI-L2-0005-RP, version 1.4.0, released 6 February 2019, KNMI, De Bilt, the Netherlands, available at: http://www.tropomi.eu/documents/atbd/, last access: 17 March 2020.

Veefkind, J. P., Aben, I., McMullan, K., Förster, H., de Vries, J., Otter, G., et. al. (2012). TROPOMI on the ESA Sentinel-5 Precursor: A GMES mission for global observations of the atmospheric composition for climate, air quality and ozone layer applications. *Remote Sensing of Environment*, 120, 70-83. doi:https://doi.org/10.1016/j.rse.2011.09.027

Verhoelst, T., Compernolle, S., Pinardi, G., Lambert, J. C., Eskes, H. J., Eichmann, K. U., et al. (2020). Ground-based validation of the Copernicus Sentinel-5p TROPOMI NO2 measurements with the NDACC ZSL-DOAS, MAX-DOAS and Pandonia global networks. Atmos. Meas. Tech. Discuss., 2020, 1-40. doi:10.5194/amt-2020-119

Vigouroux, C., Langerock, B., Bauer Aquino, C. A., Blumenstock, T., Cheng, Z., De Mazière, M., De Smedt, I. et al.: TROPOMI–Sentinel-5 Precursor formaldehyde validation using an extensive network of ground-based Fourier-transform infrared stations, Atmos. Meas. Tech., 13, 3751–3767, 2020.

Vigouroux, C., Bauer Aquino, C. A., Bauwens, M., Becker, C., Blumenstock, T., De Mazière, M., Garcıa, O. et al.: NDACC harmonized formaldehyde time series from 21 FTIR stations covering a wide range of column abundances, Atmos. Meas. Tech., 11(9), 5049–5073, 2018.

Wells, K. C., Millet, D. B., Cady-Pereira, K. E., Shephard, M. W., Henze, D. K., Bousserez, N., Apel, E. C., de Gouw, J., Warneke, C., and Singh, H. B.: Quantifying global terrestrial methanol emissions using observations from the TES satellite sensor, Atmos. Chem. Phys., 14, 2555–2570, https://doi.org/10.5194/acp-14-2555-2014, 2014.

Werf, G. R. van der, Randerson, J. T., Giglio, L., Van Leeuwen, T. T., Chen, Y., Rogers, B. M., Mu, M., Van Marle, M. J., Morton, D. C., Collatz, G. J. et al.: Global fire emissions estimates during 1997-2016, Earth Syst. Sci. Data, 9(2), 697, 2017.

Zimmerman, P., Greenberg, J. and Westberg, C.: Measurements of atmospheric hydrocarbons and biogenic emission fluxes in the Amazon boundary layer, J. Geophys. Res., 93(D2), 1407–1416, 1988.

8 Appendix: DECSO versions

The DECSO algorithm (Daily Emission estimation Constrained by Satellite Observations) has been developed for NOx emission estimation in several regions of the world and for different instruments and species. Below follows an overview of the various historical and current versions of the algorithm. A summary is given in Table 6.

Version 1

This was the first version developed by Mijling and van der A (2012). It used the regional CTM CHIMERE version 2006 with operational ECMWF data. Landuse data of the GLCF database of 1993 was used, and boundary conditions from LMDzINCA (gas) and GOCART (aerosol).

Applied in the GlobEmission project Phase 1 for NOx emissions in East Asia using GOME-2 (MetOp-A) and OMI (AURA).

Published in Mijling and Van der A (2012)

Version 2

Improvements:

- Modelling CHIMERE with sector-dependent emission injection heights
- Fast back-trajectory calculations
- Adjusted retrieval error for measured tropospheric NO2
- NOx-correlated pollutants are daily updated
- Noise and bias reduction in remote areas

Applied in the GlobEmission project Phase 1 for NOx emissions in India and South Africa using GOME-2 (MetOp-A) and OMI (AURA).

Published in Mijling et al. (2013)

Version v3a

Improvements:

- Diurnal cycle is flattened for East Asia, while the European cycle is used for other regions.
- Calculation speed is faster by switching from g95 to the ifort compiler, and calculating matrix inversions with LAPACK.

Applied in the GlobEmission project, Phase 2, for NOx emissions in East Asia, Middle East and South Africa using GOME-2 (MetOp-A) and OMI (AURA).

Note that the emission estimates showed unrealistic day-to-day (and possibly month-to-month) fluctuations of emissions. In low-emitting areas a bias in emissions is found and an unrealistic seasonal cycle when assimilating OMI measurements. That is why this version was quickly replaced by version 3b.

Not published

Version v3b

Improvements:

- CHIMERE version 2013 was implemented with new transport schemes, secondary organic aerosol chemistry, updated chemical reaction rates.
- New land use data base: GlobCover Land cover (2009).
- Biogenic emissions calculated by MEGAN
- Reduction of day-to-day emission fluctuations by applying an OmF criterium [-5,10].
- Diurnal cycle: flattened for Middle East, Rush hour included for East Asia.

Applied in the GlobEmission project, Phase 2, for upgrading NOx emissions in East Asia and the Middle East using GOME-2 (MetOp-A) and OMI (AURA).

Published in Ding et al. (2015)

Version 4

Improvements:

- Reduction of day-to-day emission fluctuations by a 3-sigma (emission error) criterion
- New parametrization of the R matrix (model, observation, representation covariances)
- OmF criterion has been removed

Applied in the GlobEmission project, Phase 2, for upgrading NOx emissions in East Asia using GOME-2 (MetOp-A) and OMI (AURA).

Not published and only shortly used because the biogenic emissions of MEGAN were not applicable to East Asia.

Version 5

Improvements:

- Switch off biogenic emissions from MEGAN in CHIMERE, to estimate the total NOx emissions instead of only anthropogenic emissions.
- Change the threshold in the sensitivity matrix of the relation between emissions and concentrations. This reduce biases coming from the uncertainties occurring at the edge of a NO_2 plume.

Applied in the GlobEmission project, Phase 2, for upgrading NOx emissions in East Asia using GOME-2 (MetOp-A) and OMI (AURA).

Published in Ding et al. (2017a) and extensively validated in Ding et al. (2017b)

Version 5.1

Improvements (especially for maritime emissions):

- Set maritime inject height of newly-found maritime emissions at 40 m.

- Excluding the observations with a large pixel size by filtering out 8 pixels at each side of the swath and excluding the observations with a cloud fraction larger than 50%

Applied in the OMI project for upgrading maritime NOx emissions in East Asia using OMI (AURA).

Published in Ding et al. (2018)

Version 5.2-TROPOMI

Improvements:

- Results are generated on 0.125 degree resolution for a smaller domain.
- Timestep of the CHIMERE decreased to 7.5 min.
- The lifetime fit of NOx has been optimized for more precise local lifetimes.
- New parametrization of the R-matrix (model, observations, representation errors) for TROPOMI
- The correlation length of Q is set to 1 km.
- Improved regularisation of the inverse calculation of (KSK+R).
- The NO2 climatology for the free troposphere has been corrected.

Applied in the SOLFEO project and H2020 project AirQast for high resolution NOx emissions in South America and West Siberia respectively using TROPOMI (Sentinel 5p).

Published in van der A et al. (2020) for West Siberia.

Version 5.2-TROPOMI-superobservations

Improvements:

- In this variant of version 5.2 (1) TROPOMI data have been regridded into super-observations before using as input and (2) Results are generated on 0.25 degree resolution. Since this version is much faster, it can calculate emissions for large regions

Applied in the ESA project ICOVAC for NO_x emissions in East Asia using TROPOMI (Sentinel 5p).

Published in Ding et al. (2020)

Table 6 Overview of DECSO versions

Version	Species	Region	Resolution (degree)	Satellite	Publication
1	NO_x	East Asia	0.25ºx0.25º	OMI, GOME-2	Mijling and Van der A, 2012
2	NO_x	India, South Africa	0.25x0.25	OMI, GOME-2	Mijling et al., 2013
3a	NO_x	East Asia, Middle East, South Africa	0.25x0.25	OMI, GOME-2	-
3b	NO_x	East Asia, Middle East	0.25x0.25	OMI, GOME-2	Ding et al., 2015
4	NO_x	East Asia	0.25x0.25	OMI, GOME-2	-
5	NO_x	East Asia	0.25x0.25	OMI, GOME-2	Ding et al., 2017a,b
5.1	NO_x	East Asia	0.25x0.25	OMI	Ding et al., 2018
5.1-NH3	NH_3	South America	0.25x0.25	IASI, CrIS	-
5.2-TROPOMI	NO_x	South America, West Siberia	0.125x0.125	TROPOMI	Van der A et al, 2020
5.2-Superobs	NO_x	East Asia, Europe	0.25x0.25	TROPOMI	Ding et al., 2020

References of DECSO

Ding, J., R.J. van der A, H.J. Eskes, B. Mijling, T. Stavrakou, J.H.G.M. van Geffen, J.P. Veefkind, Chinese NOx emission reductions and rebound as a result of the COVID-19 2 crisis quantified through inversion of TROPOMI NO2 observations, submitted to GRL, 2020

van der A, R.J., de Laat, A.T.J., Ding, J., Eskes, H.J., Connecting the dots: NOx emissions along a West Siberian natural gas pipeline, npj. Clim. Atmos. Sci. 3, 16, https://doi.org/10.1038/s41612-020-0119-z, 2020

Ding, J. van der A, R. J., Mijling, B., Jalkanen, J.-P. Johansson, L., and Levelt, P. F.: Maritime NOx emissions over Chinese seas derived from satellite observations, Geophysical Research Letters, 45. https://doi.org/10.1002/2017GL076788, 2018

Ding, J., van der A, R. J., Mijling, B., and Levelt, P. F.: Space-based NOx emission estimates over remote regions improved in DECSO, Atmos. Meas. Tech., 10, 925-938, https://doi.org/10.5194/amt-10-925-2017, 2017a.

Ding, J., Miyazaki, K., van der A, R.J., Mijling, B., Kurokawa, J., Cho, S., Janssens-Maenhout, G., Zhang, Q., Liu, F., and Levelt, P.F., Intercomparison of NOx emission inventories over East Asia, Atm. Chem. Phys.,, 17, 10125-10141, doi:doi.org/10.5194/acp-17-10125-2017, 2017b.

Ding, J., van der A, R. J., Mijling, B., Levelt, P. F., and Hao, N.: NOx emission estimates during the 2014 Youth Olympic Games in Nanjing, Atmos. Chem. Phys., 15, 9399-9412, doi:10.5194/acp-15-9399-2015, 2015.

Mijling, B. and R. van der A, Using daily satellite observations to estimate emissions of short-lived air pollutants on a mesoscopic scale. J. Geophys. Res. 117, D17, doi:10.1029/2012JD017817, 2012.

Mijling, B., R.J. van der A, R. J., and Q. Zhang, Regional nitrogen oxides emission trends in East Asia observed from space, Atmos. Chem. Phys. 13, 12003-12012, doi:10.5194/acp-13-12003-2013, 2013.